Ramona Köppl, BSc

INVESTIGATIONS ON THE AGEING RESPONSE OF A CREEP RESISTANT BARIUM CONTAINING Mg-Al-Ca ALLOY

MASTER'S THESIS

to achieve the university degree of

Diplom-Ingenieur

Master's degree programme of Advanced Material Science

submitted to

Graz University of Technology

Supervisor

Assoc.Prof. Dr.techn. Cecilia Poletti

Co-Supervisor

Dipl.-Ing. Dr.techn. Martina Dikovits

Institute of Materials Science and Welding

Graz, August 2015

"Es ist nicht genug zu wissen - man muss auch anwenden.
Es ist nicht genug zu wollen - man muss auch tun."
Johann Wolfgang von Goethe

PREFACE

First of all, I have to thank both of my supervisors, Assoc.Prof. Dr.techn. Cecilia Poletti and Dipl.-Ing. Dr.techn. Martina Dikovits for their continuous support and encouragement throughout this thesis. I really appreciate your advices and thank you for your patience. Thank you!

I would like to thank Prof. Christof Sommitsch, head of the Institute of Materials Science and Welding, TU Graz, to let me use all the facilities of the Institute.

Special thanks to Dr. Erwin Povoden-Karadeniz for providing the MatCalc database and lots of helpful discussions.

I also want to thank the Facility of Mechanical Engineering for granting me the Clever & Smart scholarship with the partner Institute for Organic Chemistry, which made the life during this study a little bit more comfortable.

Moreover, I have to thank Dipl.-Ing. Theresa Kainz (TU Graz) and Stefan Zellhofer (TU Vienna) for their help, regarding the thermal analysis.

Furthermore, I have to thank Dipl.-Ing. Dr.techn. Angelika Reichmann (FELMI) for her help regarding the SEM and EDX analysis.

A big thank you, to the whole Laboratory Team of the Institute of Materials Science and Welding. They helped me enormously with their knowledge and good advices during the experimental part of this thesis.

I have to thank my parents, my brothers and grandparents for the great support throughout my studies at TU Graz and my entire life!

Manuel, thank you for your love and patience!

AFFIDAVIT

I declare that I have authored this thesis independently, that I have not used other than the declared sources/resources, and that I have explicitly indicated all material which has been quoted either literally or by content from the sources used. The text document uploaded to TUGRAZonline is identical to the present master's thesis.

Date	Signature

Abstract

The aim of this thesis is to investigate the ageing response of the creep resistant barium containing Mg-Al-Ca alloy (ABaX422). Magnesium alloys have been widely used for lightweight applications in aerospace and automotive industries due to the lower density as compared to aluminium. The use grew until the late 70's but then greater power requirements lead to higher application temperatures for the engines. Hence, magnesium designed parts were reduced. Nowadays the weight reduction is one of the most crucial challenges in the vehicles industries. Therefore, creep resistant magnesium designed parts are of major interest.
The thesis examined the state of the art of magnesium alloys with special focus on precipitates occurring in a Mg alloy and, the different heat treatments used so far. After the description of the methodology, microstructural investigations by means of light optical and scanning electron microscopy, microindention hardness testing and differential scanning calorimetry were applied after different stages of heat treatments of the ABaX422 alloy and the results were shown. A MatCalc simulation of equilibrium phases was performed besides the experimental work. These experimental results were used to obtain first kinetic descriptions to design synchrotron diffraction tests.
The results of this thesis showed that the dendritic structure of the alloy was preserved for almost every heat treatment step. An increase in microhardness was observed at two ageing processes and the results from differential scanning calorimetric experiments were in good agreement with the equilibrium simulations. With respect to the precipitation kinetics, secondary precipitates appearing between 180°C-250°C for holding times between 10 and 120 minutes were detected by differential scanning calorimetry. Although ageing treatments did not show a huge increment in the hardness at room temperature, these precipitates may result in enhanced strength and creep resistance.
Future work has to be done on evaluating the small angle X-ray scattering (SAXS) and wide angle X-ray scattering (WAXS) synchrotron data to enhance the MatCalc database. Mechanical and creep properties on the alloys behaviour after heat treatments should be done to analyse the potential of hardening effects.

Kurzfassung

Das Ziel dieser Masterarbeit ist, das Verhalten einer als kriechbeständig deklarierten, bariumhältigen Mg-Al-Ca Legierung nach verschiedenen Auslagerungszuständen zu untersuchen. Magnesiumlegierungen wurden, aufgrund der geringeren Dichte als Aluminium, bis zu den späten 70er Jahren vermehrt in der Automobil- und Flugzeugindustrie eingesetzt, um Gewicht zu sparen. Als jedoch die Anforderungen an die Bauteile immer höher wurden, wurde der Einsatz von Magnesiumlegierungen als Baustoff wieder gestoppt, da sie den hohen Einsatztemperaturen nicht stand halten konnten. Erst durch die erneuten Anforderungen an die Gewichtsreduktion der Automobile und Flugzeuge, um Treibstoff zu sparen, sind kriechbeständige Magnesiumlegierungen entwickelt worden und auch wieder in Verwendung.
Die vorliegenden Arbeit beschäftigt sich unter anderem mit der Untersuchung der bisher veröffentlichten Literatur zu Magnesiumlegierungen. Dabei wird speziell auf die vorhandenen Ausscheidungen und die verschiedenen Wärmebehandlungen eingegangen. Im experimentellen Teil dieser Arbeit wird die Mikrostruktur der Legierung mittels Licht- und Rasterelektronenmikroskopie untersucht. Es werden auch Mikrohärtemessungen und dynamische Differenzkalorimetrie als Untersuchungsmethoden verwendet. Neben diesen experimentellen Untersuchungen, die vor und nach verschiedenen Wärmebehandlungen durchgeführt wurden, wurde auch eine Simulation im thermodynamischen Gleichgewicht mit Hilfe von MatCalc durchgeführt. Die gerade aufgelisteten Untersuchungen waren der Ausgangszustand für zusätzlich durchgeführte Synchrotron Messungen.
Die Ergebnisse der oben genannten Untersuchungen zeigten den Erhalt der dendritischen Mikrostruktur nach fast allen Wärmebehandlungen. Neben der Ausscheidungskinetik wurde der Fokus auch auf sekundäre Ausscheidungen gelegt, welche nach dem Auslagern zwischen 180°C und 250°C mit Haltezeiten von 10 Minuten bis 120 Minuten entstanden. Obwohl die Härte durch das Auslagern nicht sehr gesteigert werden konnte, wäre es doch möglich, dass die Ausscheidungen positive Auswirkungen auf die Kriechbeständigkeit haben. Des Weiteren stimmten die Ergebnisse von der dynamischen Differenzkalorimetrie gut mit den Gleichgewichtssimulationen überein.
Nichts desto trotz müssen die Ergebnisse von den Synchrotron Messungen noch weiter ausgewertet werden. In weiterer Folge sollte die MatCalc Datenbank noch verbessert und das Kriechverhalten der untersuchten Magnesiumlegierung nach den Wärmebehandlungen erneut bestimmt werden.

Content

1 Introduction 1
2 State of the art 2
2.1 Physical properties of pure magnesium 2
2.2 Magnesium alloys 3
2.3 Precipitation in magnesium alloys 5
2.4 Strengthening mechanisms 6
2.5 Heat treatments of magnesium alloys 7
2.6 Casting vs. Wrought alloy 8
2.7 Modelling of phase equilibrium and kinetics 9
3 Methodology 10
3.1 Material ABaX422 10
3.2 Sample preparation 10
3.3 Heat treatments 12
3.4 Microscopic investigations 13
3.5 Microindention hardness testing 14
3.6 Differential scanning calorimetry 15
3.7 MatCalc Simulations – Thermodynamic equilibrium 16
4 Results 17
4.1 Microstructural investigations 17
4.1.1 As-received condition 17
4.1.2 Heat treatments 18
4.2 Hardness testing 34
4.3 Differential scanning calorimetry 37
4.4 MatCalc Simulations – Thermodynamic equilibrium 41
5 Discussion 42
5.1 Phases in equilibrium 42
5.2 Precipitation kinetics 44
6 Summary and Conclusions 47
7 Outlook 48
7.1 Synchrotron experiments 49
8 List of Figures 50
9 List of Tables 52
10 Bibliography 53

1 Introduction

Magnesium alloys are good candidates for lightweight applications in aerospace, automotive, power tools and 3C (computer, communications and consumer) due to their high mechanical properties to weight ratio compared to steel and aluminium. The first automotive application of magnesium was the racing engine pistons in 1918. The use of magnesium alloys grew until the late 70's. Then, greater power requirements for the engines leaded to a reduction of magnesium designed parts since higher operating temperatures, higher loads and a good corrosion resistance were required. Nowadays, Europe is looking forward for creep resistant magnesium alloys for further weight reduction of vehicles. [1]

Generally, creep resistant magnesium alloys contain rare earth (RE) elements and aluminium as main alloying elements to promote the formation of $Al_{11}RE_3$, Al_4RE and Al_2RE precipitates [2]. However, in the last few years RE elements have been replaced by other alloying elements due to their high prices. Therefore, a new creep resistant Ba containing Mg-Al-Ca alloy was designed with higher creep resistance than the commercially used creep resistant alloys AE42 and MRI230D [3]. Although aluminium is the most common alloying element in magnesium alloys since it increases hardness and strength due to precipitation hardening and solid solution strengthening, a $Mg_{17}Al_{12}$ phase is formed [4,5], which decomposes during service above 130°C [6,7].The addition of calcium to a Mg-Al alloy results in a refinement of the as-cast microstructure, reduces the oxidation during melting, enhances the creep resistance and retards fire [8,9]. Calcium has a low solid solubility in magnesium thus forming Al_2Ca. This Al_2Ca phase is a more stable phase than the $Mg_{17}Al_{12}$ one, especially at higher temperatures [7]. Therefore a Ca content of 2 wt.% results in the suppression of the $Mg_{17}Al_{12}$ and the formation of a lamellar Al_2Ca phase. With the addition of barium, solid solution strengthening is provided due to the larger size of Ba atoms compared to the Mg ones; the radius of Ba atoms is 1.36 times larger than the one of the Mg atoms. The creep resistance of the Ba containing Mg-Al-Ca alloy (ABaX422) was tested in [3] in the as-cast condition.

In this work, the precipitation of hardening phases was characterized and described with the objective to improve the creep resistance of this alloy by means of a heat treatment. Hence, to get a better overview of the properties of magnesium alloys a literature research was performed and is summed up in the chapter "State of the art". Moreover, the "Methodology" chapter explains the used methods, while the chapter "Results" shows the data obtained at their analysis. Finally, the results are discussed and summarised. An outlook shows concepts for further work to improve the properties of the investigated alloy.

2 State of the art

This chapter starts with a short description of the physical properties of pure magnesium. The next points to be considered are magnesium alloys with special focus on aluminium, barium and calcium as main alloying elements. Due to the alloying elements, the precipitation process in magnesium is also considered besides heat treatment properties and the difference of cast and wrought alloys. The last point to be mentioned is related to the thermodynamic simulation of equilibrium phases.

2.1 Physical properties of pure magnesium

Magnesium is an alkaline earth metal and its main technological advantage for structural materials is its low density of 1.74 g/cm^3 at room temperature, which is lower as the density of aluminium (2.7 g/cm^3) [10, 11]. Magnesium has a hexagonal closed packed (hcp) lattice and a melting point of 650°C. Due to the hcp lattice, the number of slip planes is limited and therefore, its formability at room temperature is bad. Magnesium with its hcp crystal structure has one basal slip plane which can be activated in three directions. Therefore three independent slip systems are available in the hcp lattice. This low number of slip systems are the reason of the limited formability of magnesium, especially at room temperature [12]. Mg has a Young's modulus of 45 GPa and a shear modulus of 17 GPa [10], compared to aluminium with a Young's modulus of 70 GPa and a shear modulus of 26 GPa [11].

The strength of a magnesium alloy is strongly influenced by the average grain size from the Hall-Patch equation, the crystallographic texture and the second phases through dispersion and precipitation strengthening [13].

2.2 Magnesium alloys

Different alloying elements are used to improve the physical properties of pure magnesium. The designation of the alloying elements after the American Society of Testing Materials (ASTM) [4], was established to gain an overall common classification. Table 1 shows the abbreviations of the general used alloying elements.

Table 1: Alloying elements; Designation after ASTM [4]

A	Aluminium	**N**	Nickel
B	Wismuth	**P**	Lead
C	Copper	**Q**	Silver
D	Cadmium	**R**	Chromium
E	Rare Earth	**S**	Silicon
F	Iron	**T**	Tin
H	Thorium	**W**	Yttrium
J	Strontium	**X**	Calcium
K	Zirconium	**Y**	Antimony
L	Lithium	**Z**	Zinc
M	Manganese		

The barium containing Mg-Al-Ca alloy used in this work is named after the ASTM designation ABaX422, with Ba for barium. The numbers behind - "422" - represents the amount of the alloying elements in weight percent; thus, the magnesium alloy contains 4 wt.% aluminium, 2 wt.% barium and 2 wt.% calcium (detailed composition see chapter 3.1). In the following paragraphs only the influence of alloying elements aluminium, barium and calcium in the properties of Mg alloys are further described.

Aluminium is the most common alloying element in the magnesium system because it increases hardness and strength due to precipitation hardening and solid solution strengthening. The solid solution strengthening process is the result of the interaction between the elastic fields of moving dislocations and the alloying elements. Aluminium has also a positive effect on the corrosion behaviour and on the castability. In a Mg-Al alloy, the β-$Mg_{17}Al_{12}$ phase is formed as shown in Figure 1. The $Mg_{17}Al_{12}$ phase decomposes during service because of its low stability at higher temperature, decreasing the creep resistance of the material. [4, 5, 14]

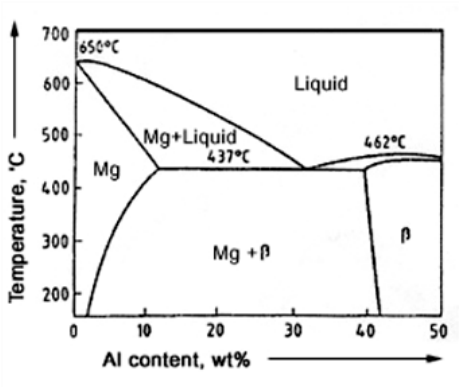

Figure 1: Excerpt of the Mg-Al binary phase diagram [15]

With the addition of **barium**, solid solution strengthening is provided due to the size of the Ba atom, that is 1.36 times larger than the size of the Mg atom.
The addition of **calcium** to a Mg-Al alloy results in a refinement of the as-cast microstructure, reduces the oxidation during melting, enhances the creep resistance and is a fire retardant[8,9]. It also leads to the formation of an Al_2Ca phase during solution heat treatment. Calcium has a low solid solubility in magnesium. Once the calcium concentration reaches a certain value, it is possible that they take the place of magnesium atoms in the $Mg_{17}Al_{12}$ phase. Therefore, a new phase will form: Al_2Ca. These phase is more stable than the $Mg_{17}Al_{12}$ phase, especially at higher temperatures [7]. Kondori et al. [6] analysed the effect of Ca addition on the as-cast microstructure from AM60. They observed, that the $Mg_{17}Al_{12}$ phase completely vanished with a Ca content of 2 wt.% and that a lamellar Al_2Ca phase was formed throughout the microstructure.
Magnesium-Aluminium-Calcium alloys contains always second phases like Mg_2Ca, Al_2Ca and $(Mg,Al)_2Ca$. These Laves phases are stable up to very high temperatures. [9], [13]

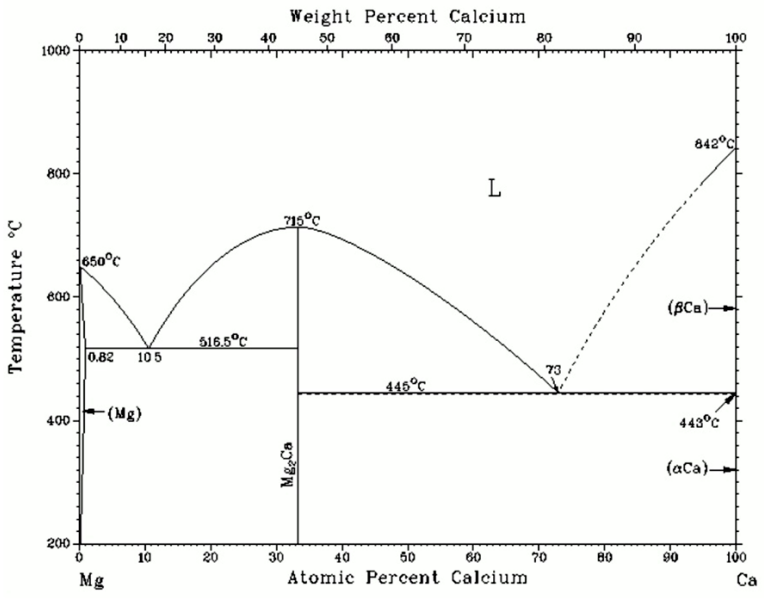

Figure 2: Mg-Ca binary phase diagram [16]

2.3 Precipitation in magnesium alloys

Laves phases are intermetallic phases with an AB_2 structure. Usually the B atom is the smaller one and the ratio of the atomistic radii is around 1.225. There are three different types of Laves phases occurring in a Mg-Al-Ca alloy and each type has its special crystal structure: the cubic $MgCu_2$-type and two hexagonal $MgZn_2$ and $MgNi_2$ types. The only difference of these three Laves polytypes is the particular stacking of the same four layered structural units. [14,17]
According to the "Strukturbericht" designation[17] the $MgCu_2$ phase is called C15, $MgZn_2$ is named C14 and $MgNi_2$, C36. The most common Laves phases are shown in Figure 3.

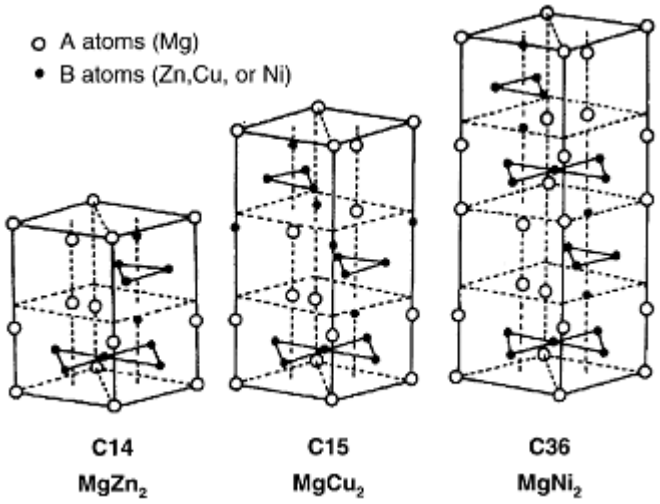

Figure 3: The three different types of Laves phases [17]

2.4 Strengthening mechanisms

Strength is the resistance in a material to plastic deformation and plastic deformation occurs by formation and movement of dislocations along the slip systems. The way to improve the strength of a material is usually to impede the dislocation movement. This can be done by work hardening, solid solution strengthening, precipitation hardening and grain boundary strengthening.
The *work hardening* process is also classified as cold working. This strengthening mechanism is carried out below the homologous temperature. During cold working, the density of dislocations and the strength increase and the ductility of the material decrease. Cell or subgrain forms, grains elongate and twins and shear bands may form. [18, 19]
Solid solution strengthening is based on the addition of alloying elements to the pure metal that remain solubilised in the original crystal structure. The alloying elements differ in size to the matrix atoms of the pure metals. The addition of different alloying elements leads to the generation of strain fields and these strain fields make the dislocation movement difficult resulting in increasing the strength of the material. [14]
Another strengthening mechanism is the *precipitation hardening*. The precipitates are separated through phase boundaries from the surrounding matrix. There are three kinds of phase boundaries which hinder the dislocation movement. When the matrix and the precipitates have the same crystal structure, then these phase boundary is called coherent. Dislocations can cut these precipitates leading to the formation of additional phase boundaries. When the matrix and the precipitates have almost same coherent boundaries, then the phase is called semi-coherent. If the crystal structure of precipitate and matrix are different in orientation and structure, then the phase boundary is named incoherent. Dislocations cannot cut incoherent precipitates but instead they can circumvent them by means of the Orowan mechanism. Depending on the size and amount of precipitates, the strength of the material reaches a maximum. [14]
The last strengthening mechanism is the *grain boundary strengthening*. Grain boundaries hinder the dislocation movement by means of pinning. Due to the fact that grain boundaries are more disordered than the grains structure inside they will prevent the dislocations from movement. The lattice structure of adjacent grains can differ and for dislocations it is more energy intensive to change their direction of movement. Therefore, more grains within a material will increase the yield strength and so the strength of a material. For an increasing effect of grain boundary strengthening a heat treatment after plastic deformation can increase the number of grains within the materials structure. [14]

2.5 Heat treatments of magnesium alloys

Three different types of heat treatments are used in practice for magnesium alloys: solution heat treatment, ageing and annealing. [20]

During a **solution heat treatment** the sample is heated up to a certain temperature at which specific constituents go into solution. Afterwards, the sample is quenched to hold these constituents in a super saturated solid solution (SSSS) condition. For a cast magnesium alloy the temperature range for solution treatment is between 340°C and 565°C with a soaking time varying between 16 and 24 hours, depending on the alloy composition [20]. Solution treatment improves strength and the maximum toughness and the shock resistance. [21, 22]
Ageing is carried out after the solution heat treatment. The quenched alloy is heated up, to promote the precipitation of the constituents held in solid solution. Therefore, a temperature range between 150°C and 260°C with usual holding times from three to six hours are suggested in [20]. The main aim of ageing is to increase the hardness and the yield strength of the alloy [21, 22].

Magnesium castings and wrought alloys achieve their mechanical properties via **age hardening**. These includes a solution treatment within the α-magnesium single phase region, water quenching to obtain a SSSS of alloying elements and a subsequent ageing, to achieve a controlled decomposition of the SSSS into a fine distribution of precipitates in the magnesium matrix. [23]
The cooling rate has a strong influence on the size and the shape of some precipitates such as the calcium containing particles. Cooling rates of 30 °C/s leads to the formation of nano scale particles. If the cooling rate decreases aluminium and calcium atoms in the liquid diffuse away from the α-magnesium dendrites towards nano calcium containing particles. They produce a fine dispersed calcium containing phase ($(Mg,Al)_2Ca$) which precipitates in the α-magnesium grains after a certain growth. The cooling rate for this process is 9.2 °C/s. A further reduction of the cooling rate to 0.5 °C/s results in the growth of the $(Mg,Al)_2Ca$ precipitates to large needle shaped ones. [24]

2.6 Casting vs. Wrought alloy

Often the question arises which manufacturing process is the better one, casting or wrought production. Wrought products (extruded bars and shapes, forgings, rolled plates or sheets) have better mechanical properties than castings, but most Mg products are castings. A short overview of the used automotive parts is given in Table 2, with respect to the manufacturing process. Magnesium alloys can be casted in numerous casting methods like sand casting, permanent and semi-permanent mold casting, investment and die-casting. Die-casting is one of the most common manufacturing processes for the production of automotive parts. Actually, the magnesium casting process is four times faster than to aluminium alloys . Special considerations must be made concerning the protective gas which is used to reduce oxygen within the furnace. Magnesium produces a permeable oxide layer on the surface of the molten magnesium alloy. Therefore, oxygen can pass through, and burning starts underneath the oxide layer. Magnesium castings have also a similar shrinkage than aluminium castings. On the contrary, wrought alloys are easy to machine and have a higher dimensional stability. Since iron has a low solubility in molten magnesium alloys, steel crucibles or steel tools can be used in the manufacturing process. [25, 26, 27, 28]

Table 2: Some automotive components made of magnesium wrought alloys [27]

System	Component	Manufacturing process
Interior	Instrument panel	Extrusion or high pressure die-casting
	Seat components	Extrusion or sheet
Body	Door inner	Sheet
	Roof frame	Extrusion
	Sunroof panel	Sheet
Chassis	Wheel	Forging
	Subframe	Extrusion

2.7 Modelling of phase equilibrium and kinetics

The best way to describe the equilibrium state of a system is the Gibbs free energy **G** [29]. The Gibbs energy is dependent on temperature T, pressure P and chemical composition N, variables that can be controlled in experimental setups [30].

$$G(T,p,N) = H(S,V,N) - TS$$

If a system is held at constant temperature and pressure, the system reaches the minimum value of G by approaching an equilibrium state [29].

Typical applications of thermodynamic equilibrium calculations are the determination of phase- and phase fraction diagrams, non-equilibrium calculations and Scheil-Gulliver simulations. The Scheil-Gulliver method consists on the calculation of fraction and composition of phases in the alloy, from the liquidus temperature to the solidification temperature [31].
There are several commercial products available for thermodynamic calculations e.g. FactSage, MTDATA, PANDAT, JMatPro, Thermo-Calc and MatCalc. The MATerials CALCulator, *MatCalc* [32], is a software based on the CALPHAD method for simulation of thermodynamic and kinetic phases, precipitation and dissolution.
According the databases, a Mg-based alloy database is available from Thermo-Calc [33], that includes 24 alloying elements: Ag, Al, Ca, Ce, Cu, Fe, Gd, K, La, Li, Mg, Mn, Na, Nd, Ni, Pr, Sc, Si, Sn, Sr, Th, Y, Zn, Zr but Ba is missing. Due to this, a new database was developed within this thesis: a Mg-Al-Ca-Ba database.

3 Methodology

This chapter consists of seven subchapters starting with general information of the investigated material and the sample preparation. After that, the description of various used heat treatments is accomplished. The experimental part of this thesis is further divided into metallographic investigations followed by hardness testing and concluded with the thermal analysis of the material. Five different examination techniques were used to characterize the microstructure of the alloy: LOM, scanning electron microscope (SEM), energy dispersive X-ray spectroscopy (EDX), microindention hardness testing and differential scanning calorimetry (DSC). Thermal equilibrium calculations were performed to obtain information of the hardening phases.

3.1 Material ABaX422

ABaX422 is a new Mg alloy developed to be creep resistant. The Mg alloy was provided by the *Magnesium Innovation Centre* (MagIC), *Institute of Materials Research* of *"Helmholtz Zentrum Geesthacht"*.

The alloy was produced by melting highly purified magnesium (99.99%), pure aluminium (99.9%), barium (>99.0%) and calcium (99.5%). The chemical composition of the Mg alloy is shown in Table 3. Mn and Sr were found as impurities. The temperature of the liquid alloy was held at 720°C and stirred over 10 minutes to produce a homogeneous distribution of the alloying elements. The molten alloy was then casted in an ingot mold preheated at a temperature of 300°C. The mold was lowered into a water bath immediately after the casting process. Solidification starts on the bottom of the mold but to obtain a defect free microstructure some liquid alloy is still poured onto the solidification front. [3,34]

Table 3: Composition in weight percent ABaX422 [3, 34]

Mg	Al	Ba	Ca
Base	4.25	1.50	1.51

3.2 Sample preparation

The material provided from MagIC was delivered after solidification and uncontrolled cooling, without any heat treatment. This state of the material is called "as-received" condition. The alloy was supplied as cylinder, with a diameter of 10 cm and a height of 15 cm. For all further measurements the samples were worked out from this cylinder. The specimens for metallographic investigations and for hardness measurements were cuboids of 5 x 5 x 10 mm. For the thermal analysis in a DSC device (see chapter 3.6) two different sample sizes were required, depending on the used facility. According to the Netzsch 409c device, cylindrical samples with a diameter of 5 mm and a height of 5 mm were

produced. The TA-Instruments Q2000 required disc-shape samples with a diameter of 5 mm and a height of 1 mm.
The microstructure of all samples was analysed. Therefore, the samples were embedded in Technovit® 4071 resin, a cold polymerizing resin for metallographic investigations. Afterwards, grinding and polishing were done with the semi-automatically machine Struers Tegramin-30 with the parameters listed in Table 4.

Table 4: Steps for grinding and polishing

	Consumables	Lubricant	Time [min]	Force [N per sample]
Grinding	SiC paper 320	Water	1.5	10
	SiC paper 500		1	
	SiC paper 800		1	
	SiC paper 1200		1	
	SiC paper 2000		1	
	SiC paper 4000		1	
Polishing	MD-Mol 3 µm	3 µm	3	
	MD-Mol 1 µm	1 µm	2.5	
	MD-Chem OPS	OPS	3	
	MD-Chem OPS	Water	5	

Polishing with OPS was done over a period of time of 3 minutes. Since Mg alloys reacts easily with the OPS lubricant, 5 minutes of polishing with water was applied after the OPS-step. The samples were cleaned after each grinding and polishing step with water followed by ethanol.

The samples were etched to examine the microstructure under the light optical microscope (LOM). Picric acid was used (see Table 5) for 10 seconds.

Table 5: Chemical composition of the etchant

10 ml distilled water
70 ml ethanol
10 ml acetic acid (80%)
4.2 g picric acid

3.3 Heat treatments

Heat treatments were carried out as shown in the sketch in Figure 4. The first step was a homogenisation heat treatment, realized in the furnace Nabertherm HTC 08/14 under normal atmosphere. The furnace was heated up to 500°C for a soaking time of 24 hours, followed by air cooling. The objective of this heat treatment was to homogenize the alloying elements in the sample and to get rid of any micro-segregation. Additionally, the stability of the interdendritic phases was observed.
Solution and ageing treatments were both carried out in the dilatometer Bähr DIL-805A/D to get a good control of the temperature, heating and cooling rates, better than in a furnace. These two heat treatments were carried out successively for each sample. "Typ S" thermocouples welded at the sample's surface were used for the temperature measurement. The samples were heated up to 520°C with a heating rate of 10 °C/s and held for 1 hour. Immediately at the end of the holding period the sample was cooled down with helium. Thereupon, the samples were heated up to the individual ageing temperatures with 10 °C/s and held for different ageing times, as shown in Table 6. At the end of the ageing process the heating was switched off to simulate a free cooling process. Air was used during the test and no oxidation of the material was detected. Table 6 shows a summary of the heat treatments.

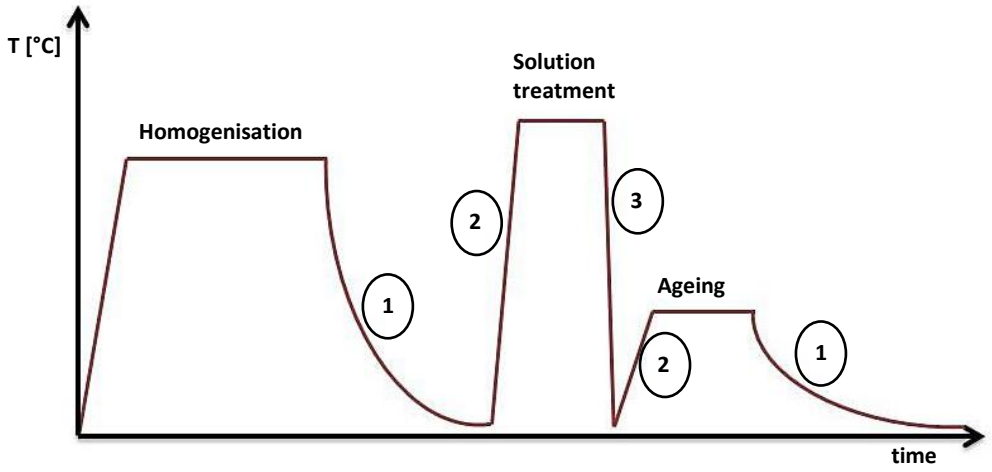

Figure 4: Sketch of the heat treatment cycle consisting of homogenisation (500°C, 24 hours), solution treatment (520°C, 1 hour) and different ageing processes; Number 1 indicates free cooling, 2 indicates a heating rate of 10 °C/s, 3 represents quenching with helium

Table 6: List of heat treatments

	Temperature [°C]	Duration [min]	Cooling medium
Homogenisation	500	1440	air
Solution treatment	520	60	helium
Ageing	180	10	air
		30	
		80	
		120	
	200	10	
		30	
		80	
		120	
		180	
	250	10	
		30	
		80	
		120	
	300	10	
		30	
		120	

3.4 Microscopic investigations

Light optical microscopy is the method with the lowest requirements to sample preparation and used for first investigations of the microstructure with a maximum magnification of 1500x. LOM investigations were carried out to get basic informations of the dendritic structure. The microstructural investigations were done using a Zeiss Axio Observer.Z1m microscope, and pictures were taken with the camera AxioCam MRc5 (Zeiss). Additionally, it is possible to get many pictures in the Z-direction focused at different Z-positions. The computer program generates then one picture out of these pictures and they are further designated as "Z-stacking" images.

The scanning electron microscope is a powerful tool to investigate microstructural features and chemical compositions by EDX. The measurements were done using two different microscopes: a FEI Quanta 200 and a Zeiss Ultra[55]. An acceleration voltage of 10 kV was used in both microscopes. The main differences of the microscopes are the resolution and the available electron detectors. With the FEI Quanta 200 a resolution of 3 nm at 30 kV and 10 nm at 3 kV can be obtained [35]. To gain information of the sample's topography, secondary electrons (SE) were detected with an Everhart-Thornley detector. For the material contrast, back

scattered electrons (BSE) were detected with a Solid State detector. The determination of elemental composition and acquisition of elemental maps of was done with a Silicon-Drift detector from EDAX. On the other hand, the Zeiss Ultra[55] has a resolution of 1 nm at 15 kV and 1.7 nm at 1 kV and different electron detectors [36]. The Everhart-Thornley detector was used for the detection of the SE and an Angle Selective BSE detector for the BSE. The EDX analysis was done with an EDAX Phoenix detector.

3.5 Microindention hardness testing

With this measurement technique it is possible to measure the hardness of a material at a microscopic scale. The hardness of the metallic matrix was measured to obtain indirect information of the precipitation state.
The microindention hardness tests were performed for the following samples: as-received, solution treated and aged condition, as described in chapter 4.1.2.3.
Phases with different colours were noticed during the LOM investigations as shown in Figure 5. For the hardness measurements each phase was investigated separately and at the end a mean value of the samples hardness was calculated.

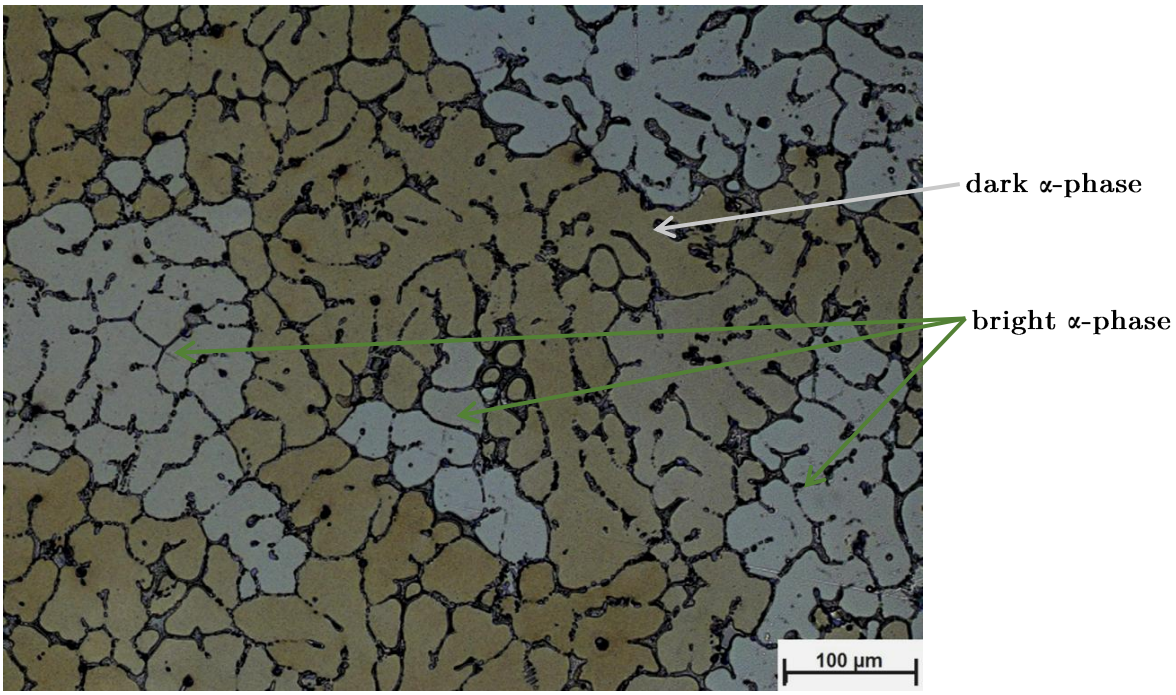

Figure 5: Specification of the bright and dark phases for hardness measurements; sample condition: ageing at 250°C for 80 min

Five hardness measurements were made at each α-phase. Then a mean value and a standard deviation were calculated for the bright and dark phases. In order to calculate a mean value for both phases, the hardness values of the bright and dark phases were averaged.
In this study, a Vickers pyramid was used for the microindention hardness testing. The term "mirco" is referred to the low load that is applied during the testing process. For ABaX422 a load of 0.05 N over a period of time of 30 seconds was used on the MHT-4 Microhardness Tester from Paar.

3.6 Differential scanning calorimetry

DSC is a powerful tool for the analysis of thermal aspects but also for investigations on precipitation kinetics. It is applicable to a variety of materials and it provides both qualitative and quantitative informations. During DSC measurements a difference in the heat flow is measured between the sample and an inert reference material. Some reasons for the wide field of its use are the easy sample preparation, the time-saving factor due to fast measurement cycles and a wide temperature range for measurements, besides the characteristic of being an "in-situ" measurement. On the other hand, the results are sometimes difficult to interpret due to overlapping of different types of phenomena. [37]

Two types of DSC were used for the analysis of ABaX422, a Netzsch 409c and a Q2000 from TA-Instruments. The second one has a better resolution in the lower temperature regime. Samples were positioned inside graphite crucibles and MgO_2 was used as reference material for the measurements realized with Netzsch 409c. In the Q2000, the measurements were done against air as reference. A heating rate of 10 °C/min was used in both DSC's. With the Netzsch 409c a temperature range of 25°C-600°C was investigated, while a temperature range of 25°C-500°C was used for the Q2000.

The measurements were done to characterize the precipitation state of different heat treated samples. There is a direct connectivity between the phase transition and the heat flow type occurring in the DSC analysis (see Table 7). The heat flow is defined as exothermic and endothermic. Exothermic means, that energy (heat) will be released from the system during the reaction (e.g. crystallization and phase precipitation). On the contrary, endothermic means that heat is brought into the system during the reaction which is the case of decomposition and melting of phases. In Table 7 a short list of conversions according to the heat flow is shown.

Table 7: Connectivity between phase transition and peak direction [38]

Conversion	Heat flow	
	Endothermic	*Exothermic*
Melting	×	-
Crystallization	-	×
Dissolution	×	-
Precipitation	-	×

3.7 MatCalc Simulations – Thermodynamic equilibrium

The MatCalc version 5.60.1003 was used to calculate equilibrium phases using a specially developed database for the ABaX422 alloy. The database is still under progress at the TU Vienna.
The chemical composition for the simulations of the alloy is shown in Table 8.

Table 8: Composition in weight percent for thermodynamic equilibrium calculation

Mg	Al	Ba	Ca
Base	4.25	1.50	1.51

The following phases were chosen for the equilibrium calculations (Table 9):

Table 9: Phases considered for equilibrium calculations and their MatCalc designation

Equilibrium Phases	MatCalc designation
Liquid	Liquid
α-Mg	F$HCP_A3
$Mg_{21}Al_3Ba_2$	F$M21A3B2
$(Mg,Al)_2Ca$	F$LAV_C36
Al_2Ca	F$LAV_C15
$Mg_{17}Al_{12}$	F$G_AL12MG17

Stepped equilibrium calculations were performed from 25°C to 700°C to gain information about both, the phases in equilibrium and the solvus temperature.
Furthermore, the phases after homogenisation treatment were of great interest. Therefore, an equilibrium calculation was performed at 500°C. Afterwards, the composition of the α-Mg phase (see Table 10) was used to perform second MatCalc equilibrium calculations to get information of the precipitates in the matrix between 25°C and 700°C.

Table 10: Composition of α-Mg in weight percent after the equilibrium calculation at 500°C

Mg	Al	Ba	Ca
Base	2.503	0.001	0.112

4 Results

The results are shown in the same order as the experimental chapter. The results of microstructural evaluation followed by hardness testing and the thermal analysis are firstly shown. Finnaly, the phase equilibrium simulations are shown.

4.1 Microstructural investigations

The microstructure after different heat treatments are shown, starting with the as-received condition, followed by homogenized, solution treated and aged conditions.

4.1.1 As-received condition

Figure 6 shows an overview of the dendritic microstructure in the as-received condition. According to picture c) in the Z-staking mode, the additional inter-dendritic phases are shown. The dendrites consist of α-Mg. The two inter-dendritic phases are the Ba-rich and a Ca-rich phases as explained in the work from Klein et al. [39]. The Ca-rich phase tends to precipitate as a lamellar, eutectic Al_2Ca phase (see Liu et al. [40]). On the other hand, the bulky Ba-rich phase is $Mg_{21}Al_3Ba_2$ as explained in the work of Dieringa et al. [3].

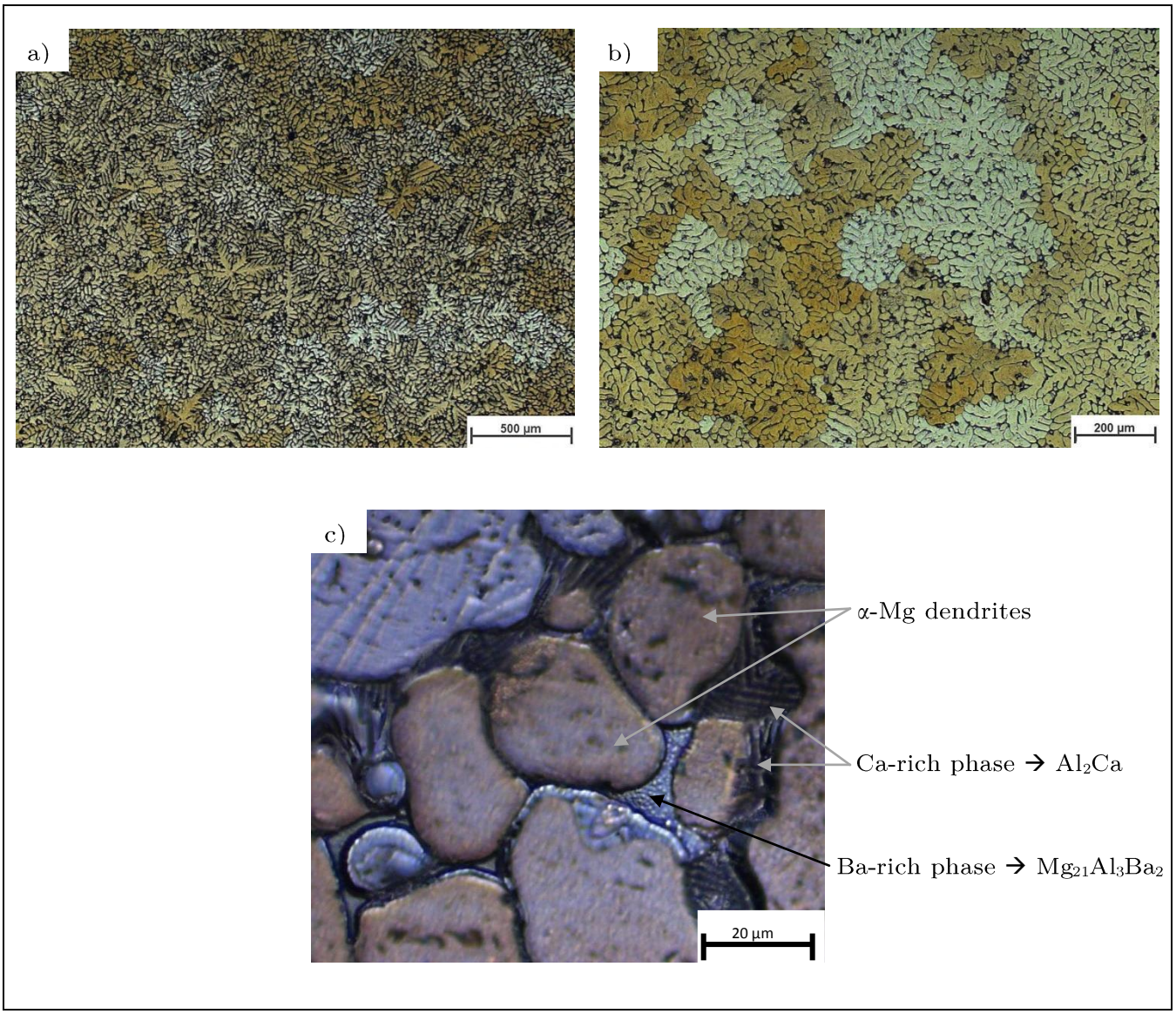

Figure 6: a) and b) Material in the as-received condition; c) Z-stacking image of as-received condition

4.1.2 Heat treatments

This chapter is divided into three different parts according to the single steps of the heat treatment: homogenisation, solution treatment and ageing.

4.1.2.1 Homogenisation

Homogenisation was done for 24 hours at 500°C in the furnace Nabertherm HTC 08/14. The dendritic structure was preserved (Figure 7 a), but the $Mg_{21}Al_3Ba_2$ phase became finer as in the as-received condition. The finer $Mg_{21}Al_3Ba_2$ phase can be seen in Figure 7 b (Z-stacking mode).

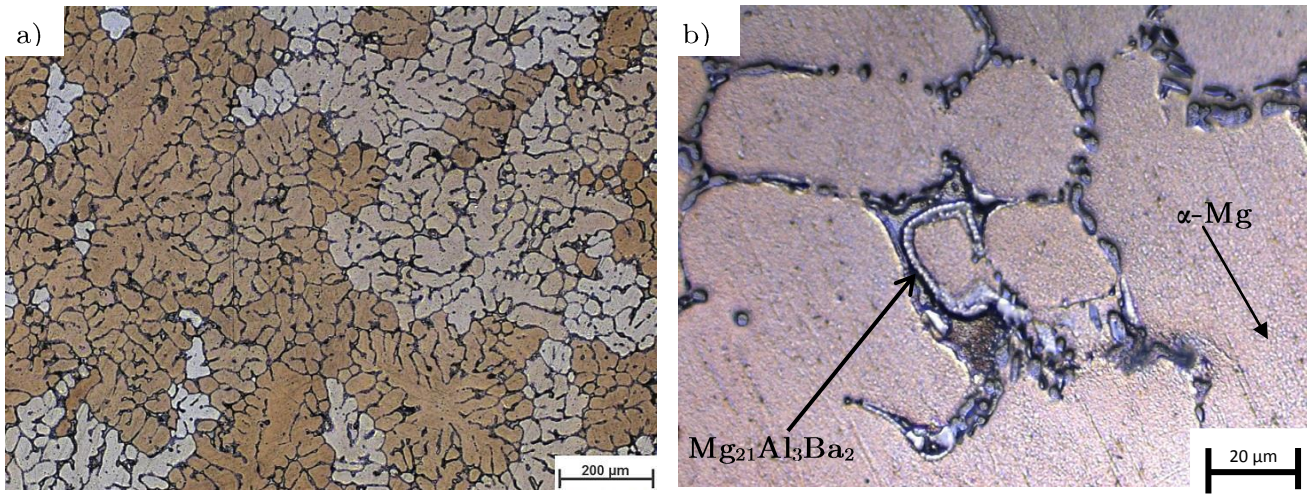

Figure 7: a) Material after homogenisation heat treatment; b) Z-stacking image of as-received condition

This homogenisation heat treatment was performed for every sample which runs through further heat treatments.

4.1.2.2 Solution treatment

The best solution treatment process, according to temperature and time (see Table 11) was the result of many experiments performed in the furnace Nabertherm HTC 08/14. Samples were cooled down with water quenching.

Table 11: Temperature and time of various solution treatments tested in the furnace

t [min] / T [°C]	5	10	30	60	480
500			×	×	×
520				×	
535			×		
550	×	×	×		

The solution treatments at 550°C over a period of time of 5, 10 and 30 minutes showed melted and re-solidified phases. The samples which were solution treated at 535°C showed the same features as the samples treated at 550°C. At both temperatures the dendritic structure was replaced by a more globular structure as can be seen in Figure 8 and Figure 9.

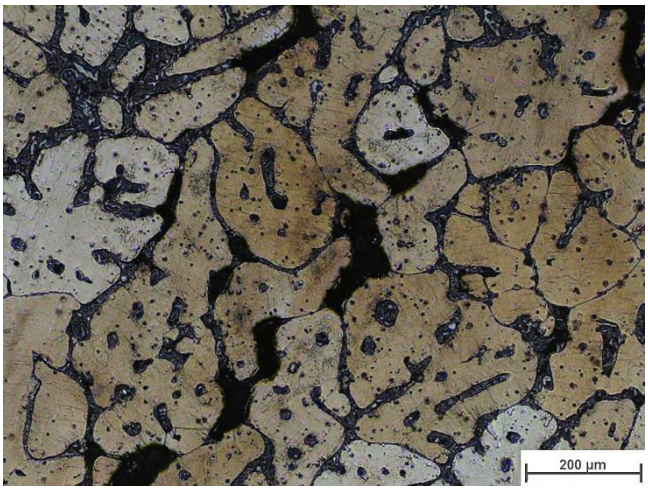

Figure 8: Solution treatment at 550°C for 30 min

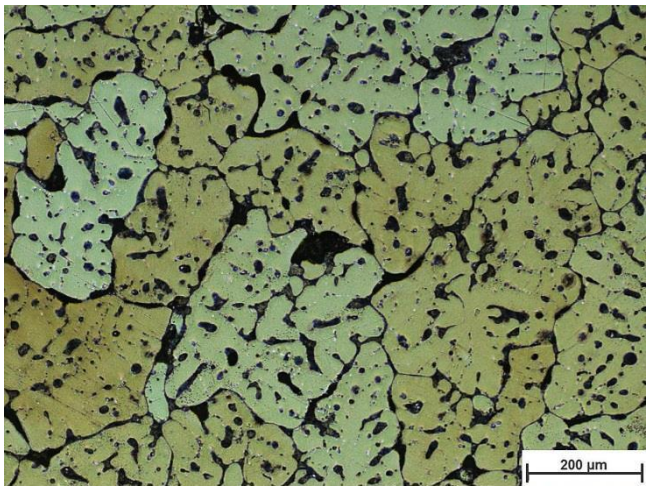

Figure 9: Solution treatment at 535°C for 30 min

The samples with a solution treatment for 60 minutes at 520°C and 500°C retained the dendritic structure of the as-received condition. The inter-dendritic spacing was wider than in the as-received condition (compare Figure 10 or Figure 11 with Figure 6). Re-solidified phases were not observed.

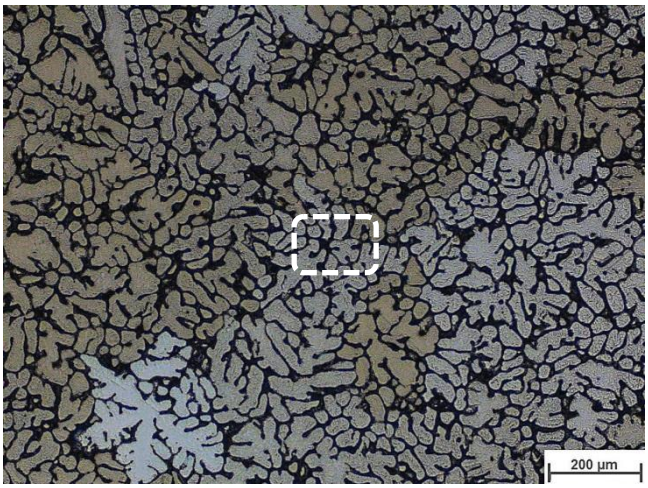

Figure 10: Solution treatment at 520°C for 60 min; marked area for zoom (see Figure 12)

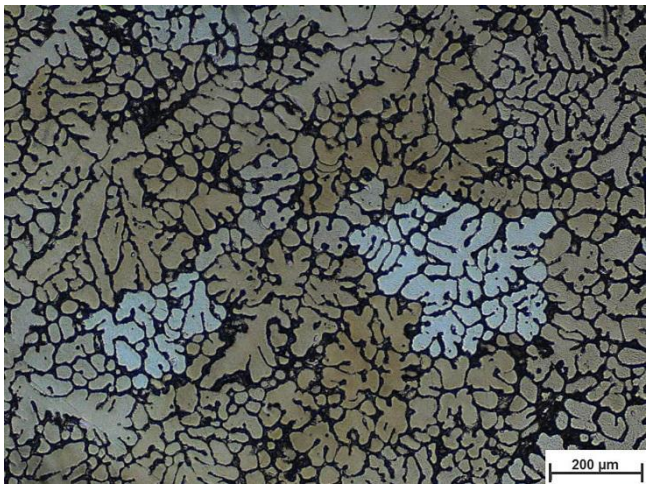

Figure 11: Solution treatment at 500°C for 60 min

The marked area in Figure 10 is shown in Table 12. The inter-dendritic Ca-rich region is observed in detail. The roughness of the surface is a result of the etching process. The picture was taken with LOM in the Z-stacking mode (see chapter 3.4).

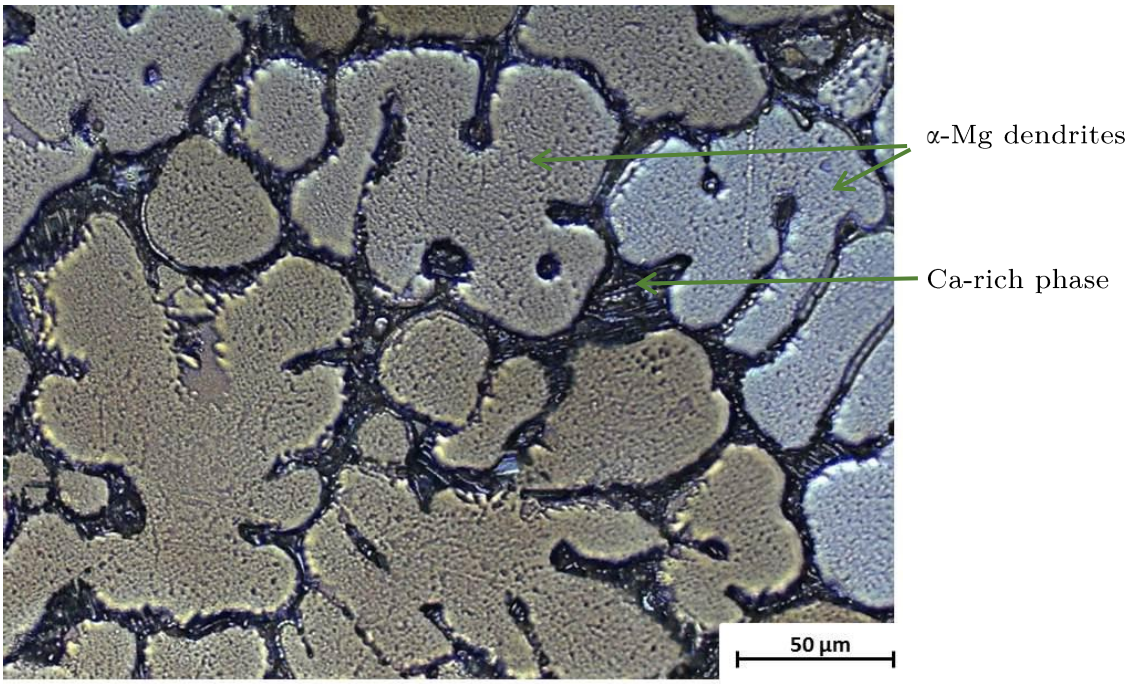

Figure 12: Marked area from Figure 10; Z-stacking mode

An additional investigation of the cooling process [24] was done besides the variation in temperature and time. For these experiments, all samples were held for 60 minutes at 520°C. The LOM examinations were performed after three different cooling rates and three dissimilar cooling mediums: water quenching, a free cooling in air and a cooling within the furnace.
After solution treatment at 520°C for 60 minutes and a free cooling in air, as it is shown in Figure 13 and Figure 14, the dendritic structure was preserved.

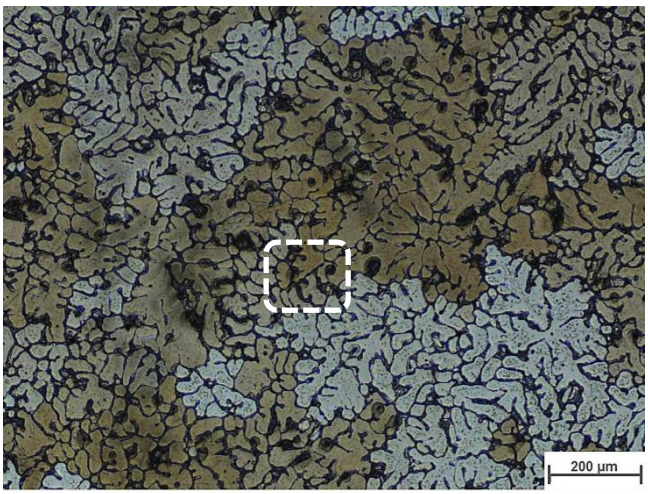

Figure 13: Solution treatment for 60 min at 520°C; free cooling in air; marked area for zoom (see Figure 14)

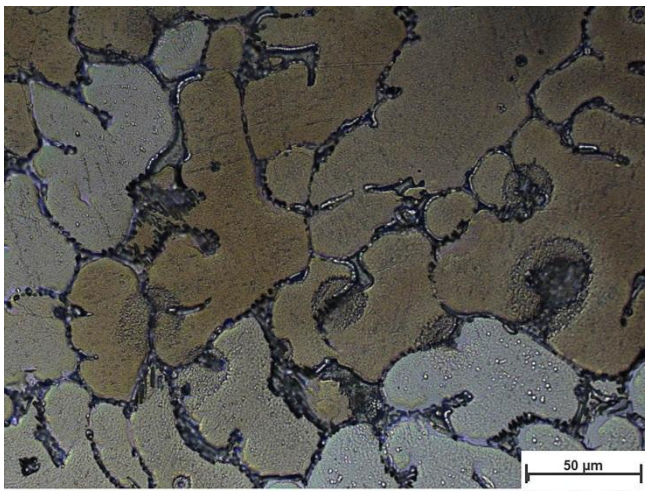

Figure 14: Zoom of marked area in Figure 13

On the other hand, during the cooling process within the furnace, new phases were formed in the α-dendritic structure. The samples were solution treated and after a soaking time of 1 hour the furnace was switched off. The samples stayed in the furnace until the furnace cooled down at room temperature. Figure 16

shows SEM and EDX analysis after furnace cooling and new needle shaped precipitates were observed, as shown in Figure 17.

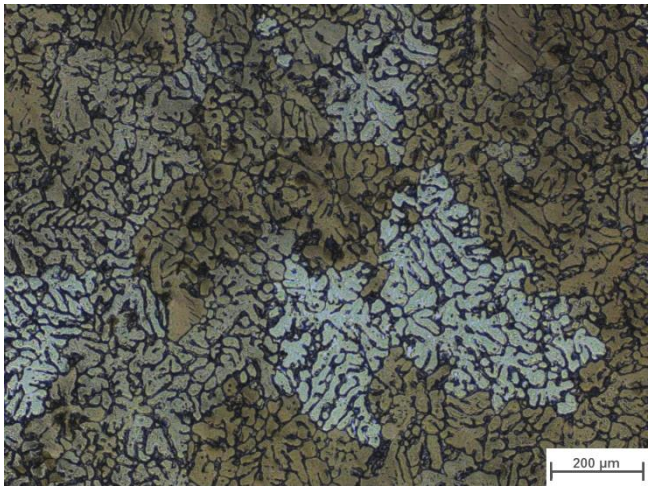

Figure 15: Solution treatment for 60 min at 520°C; cooling in the furnace

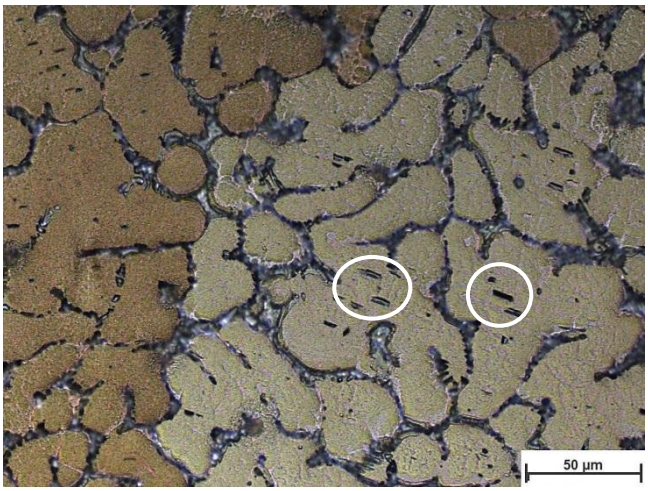

Figure 16: New needle shaped precipitates after a solution treatment at 520°C for 60 min; cooling in the furnace

SEM investigations of the needle shaped precipitates from Figure 16 were performed. The topographic information of the sample can be seen in Figure 17. The light grey phases are Al-, Ca-rich phases, indentified as Al_2Ca phases and, the dark grey region corresponds to the α-Mg phase. The different grey values in Figure 18 indicate a different chemical composition of the present phases.

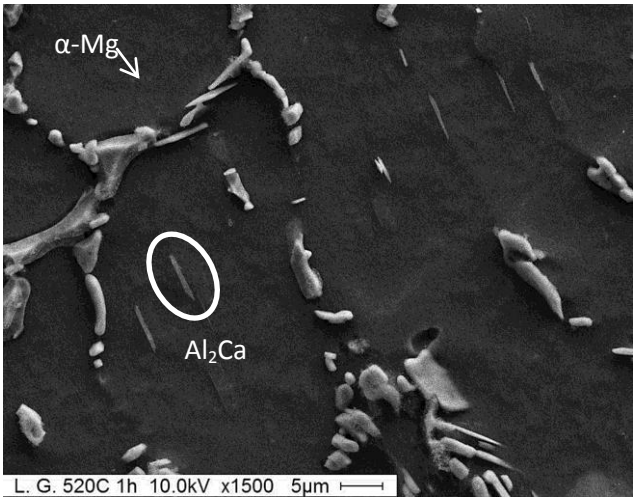

Figure 17: Solution treatment for 60 min at 520°C, cooling within the furnace; SE image

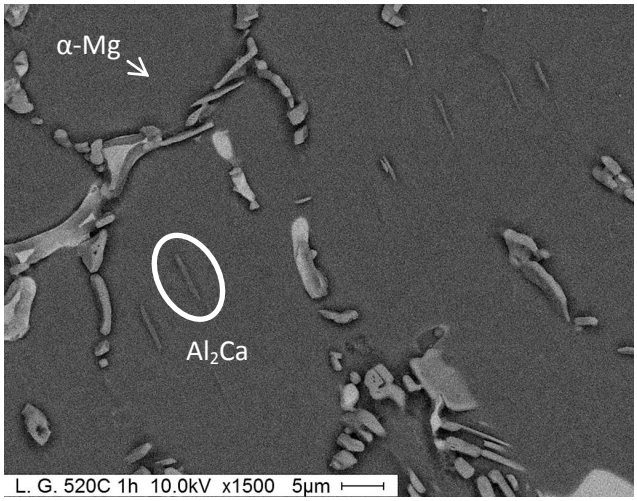

Figure 18: Solution treatment for 60 min at 520°C, cooling within the furnace; BSE image

For further analysis of the sample, images with the AsB detector were taken to gain resolution in the BSE mode. Within Figure 19 four positions were tagged, where EDX analysis were performed. Position 1 in Figure 19 indicates the appearance of the Ba-rich phase ($Mg_{21}Al_3Ba_2$), Position 2 is the confirmation of the Ca-rich phase (Al_2Ca) and Position 3 shows that the dendrites consist almost

of pure α-Mg. On the other hand, the amount of Mg which is present in the EDX scan in Position 4, indicates that the needle shaped precipitates can be the $(Mg,Al)_2Ca$ phase, too. It is also possible, that these precipitates corresponds to the Al_2Ca phase, and that the amount of Mg measured is due to the penetration depth (1 µm penetration depth for 10 kV) of the electron beam to the base material underneath the needles. The carbon peaks in all four EDX scans were the result of the used carbon tape, which was applied to reduce the electrostatic charging of the sample. The oxygen peaks appeared as a consequence of oxidation.

Besides the SEM analysis of the sample, an additional EDX mapping was made from Figure 18, as shown in Figure 20. Aluminium, calcium and barium are distributed in the inter-dendritic phases. Al and Ca also agglomerate in the needle shaped phase formed in the dendrites. When comparing the barium phases in Figure 19 and Figure 20 it can be seen, that the Ba content in Position 1 is in good correlation with the Ba-mapping in Figure 20.

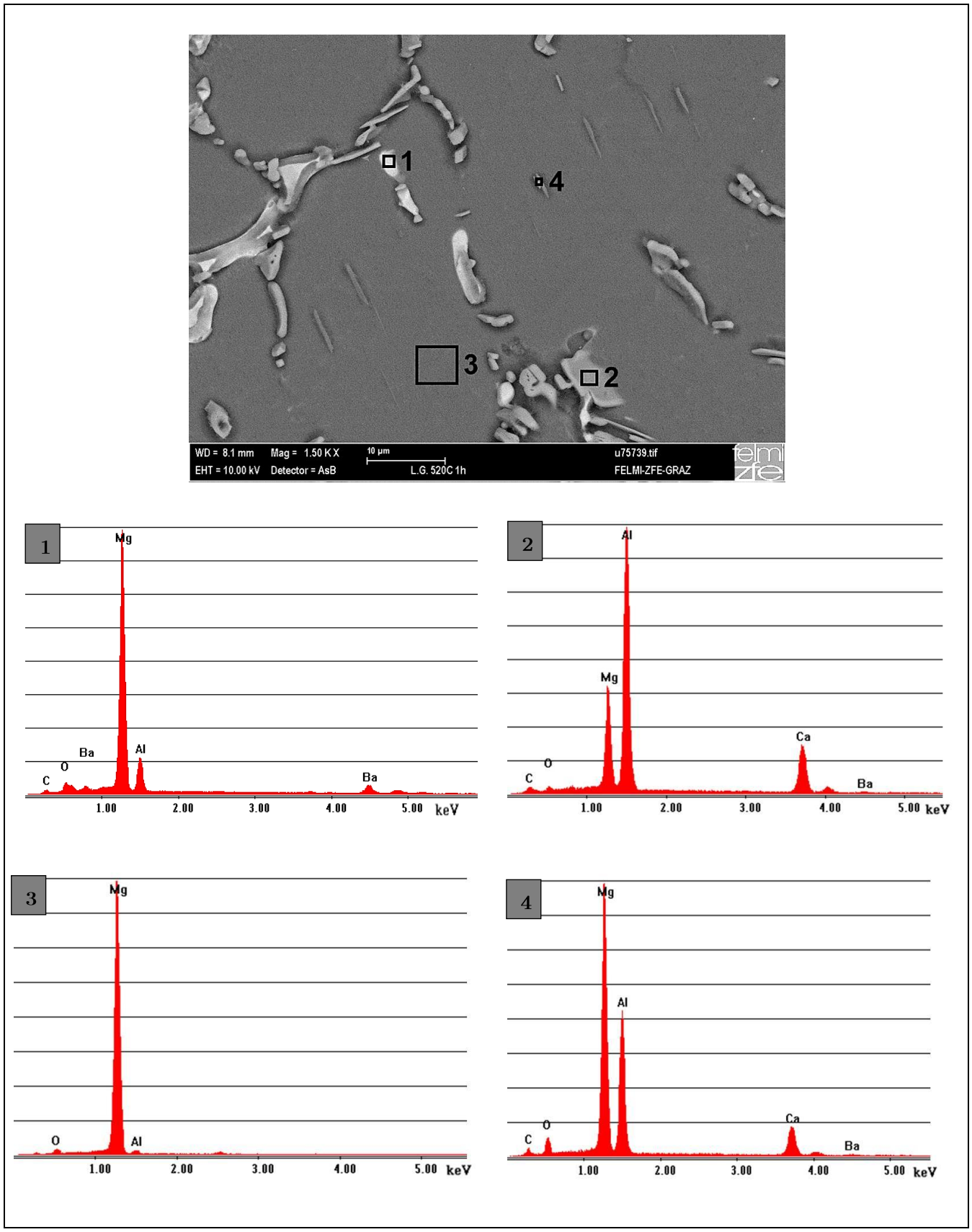

Figure 19: BSE image; solution treated for 60 min at 520°C and EDX scans from the marked positions; x-axis: energy [keV], y-axis: intensity [a.u.]

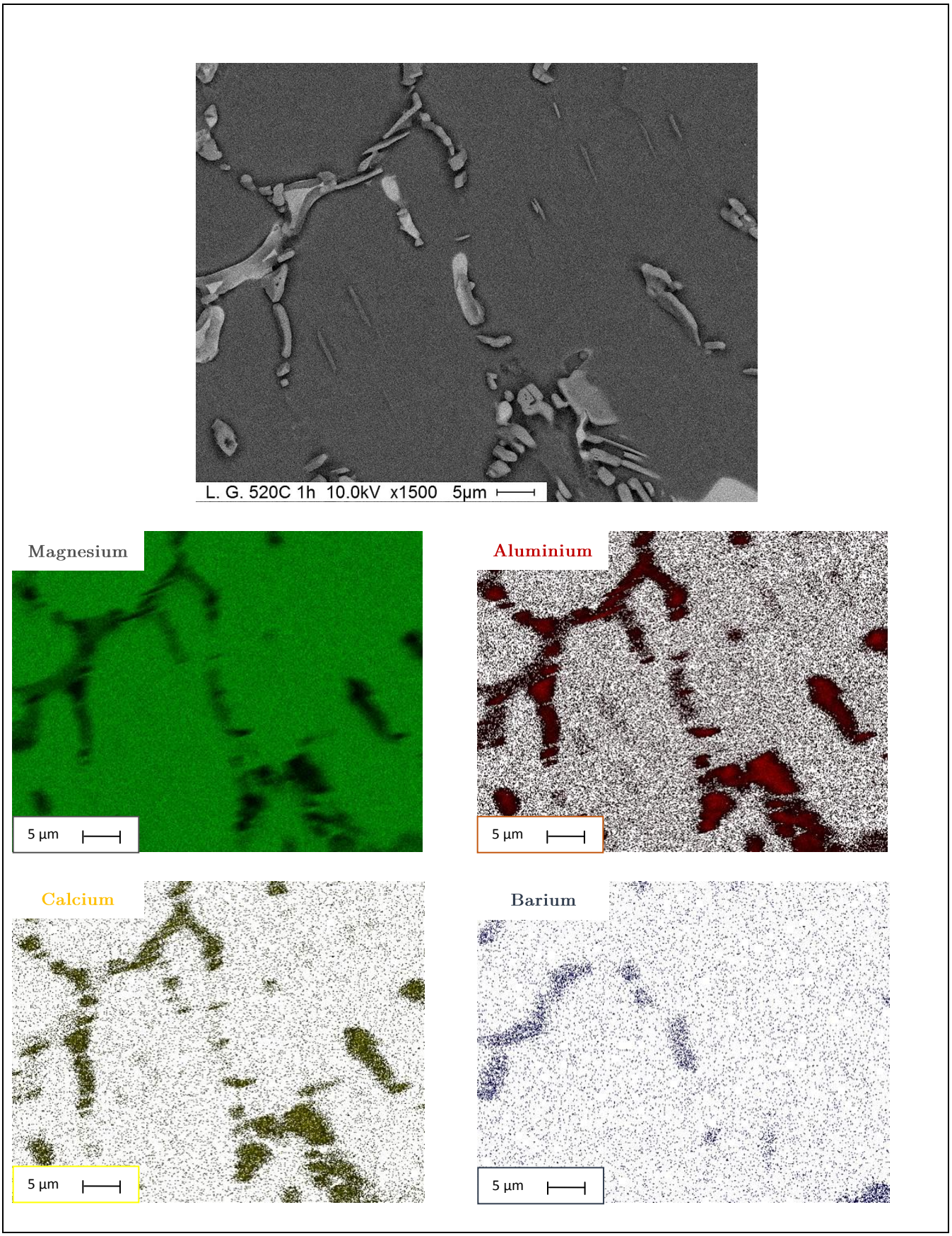

Figure 20: EDX mapping and BSE image from the solution treated sample (for 60 min at 520°C)

The sample solution treated at 550°C for 30 minutes was also analysed (see Figure 21 and Figure 22). The material contrast is shown in Figure 22. The dark grey phase is α-Mg, the middle grey colour stands for the Al_2Ca phase and the light grey indicates Ba. The small dots in Figure 21 were artefacts from the polishing process and have no correlation with the precipitates.

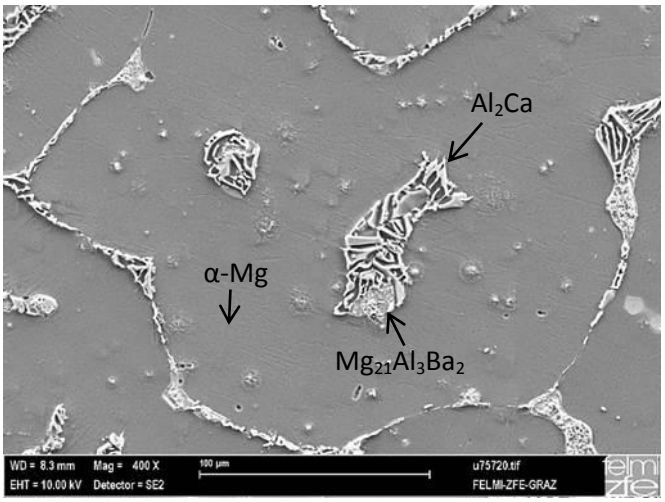

Figure 21: Solution treated sample for 30 min at 550°C; SE image

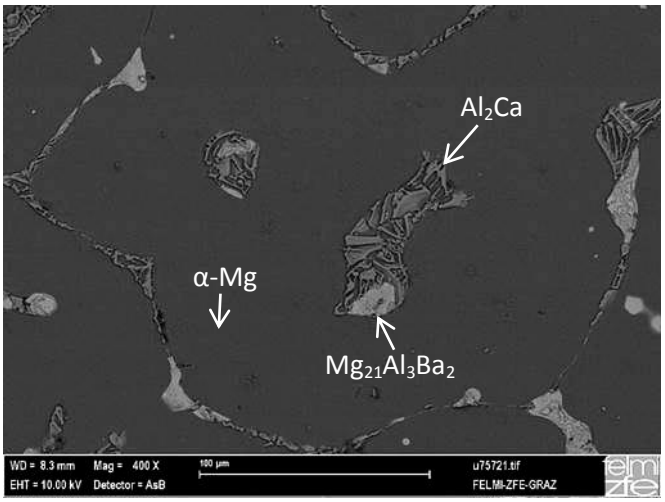

Figure 22: Solution treated sample for 30 min at 550°C; BSE image

The EDX scans from the solution treated sample (550°C for 30min) are shown in Figure 23. Position 1 in Figure 23 indicates the presence of α-Mg phase in between the Al_2Ca phase, and Position 2 refers to the Ba-rich phase. The silicon peak in the EDX scan occurs due to the grinding with SiC paper (see chapter 3.2.).

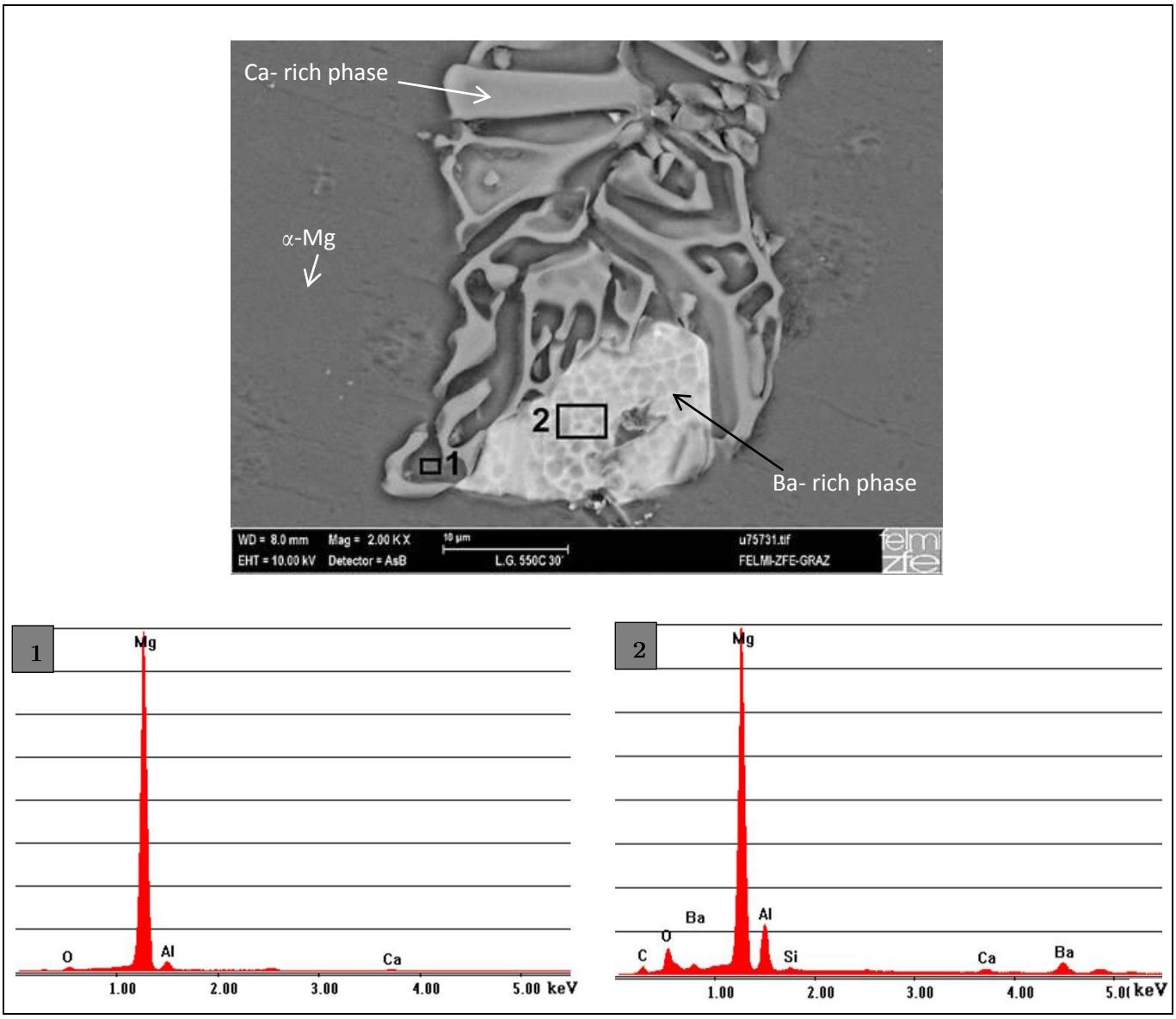

Figure 23: EDX scan from the solution treated sample (550°C for 30 min); BSE image and EDX scans from 1 and 2; x-axis: energy [keV], y-axis: intensity [a.u.]

A summary of the solution treatments is shown in Table 12. The effect of different holding times and temperatures on the microstructures can be clearly seen. Due to the partial melting of phases at 550°C and 535°C any of these two temperatures were not used for the solution treatment process. The solution treatment at 500°C showed no change in the microstructure. The solution treatment at 520°C for 60 minutes and the cooling in the furnace confirmed the occurrence of second phases. These second phases are crucial for the following ageing process when achieving fine precipitates. Therefore, the solution treatment used in further tests was at 520°C over 60 minutes.

Table 12: Summary of the different solution treatments tested

T [°C]	t [min]	cooling medium	changes in the microstructure	dendritic structure	globular structure
500	30	water	-	×	-
	60	water	-	×	-
	480	water	-	×	-
520	60	water	-	×	-
		air	-	×	-
		furnace	needles within α-Mg	×	-
535	30	water	melted phases	-	×
550	5	water	melted phases	-	×
	10	water	melted phases	-	×
	30	water	melted phases	-	×

For all the following chapters, the heat treatment at a temperature of 520°C for 60 minutes will be refer as solution treatment.

4.1.2.3 Ageing

Ageing treatments were carried out after homogenisation, solution treatment and quenching with helium. The first ageing treatment was carried out at ***180°C*** for 10, 30, 80 and 120 minutes. In Figure 24 the remaining dendritic structure is visible for three of the four time steps. On the left hand side always a magnification of 100x, whereas on the right hand side a magnification of 500x was used.

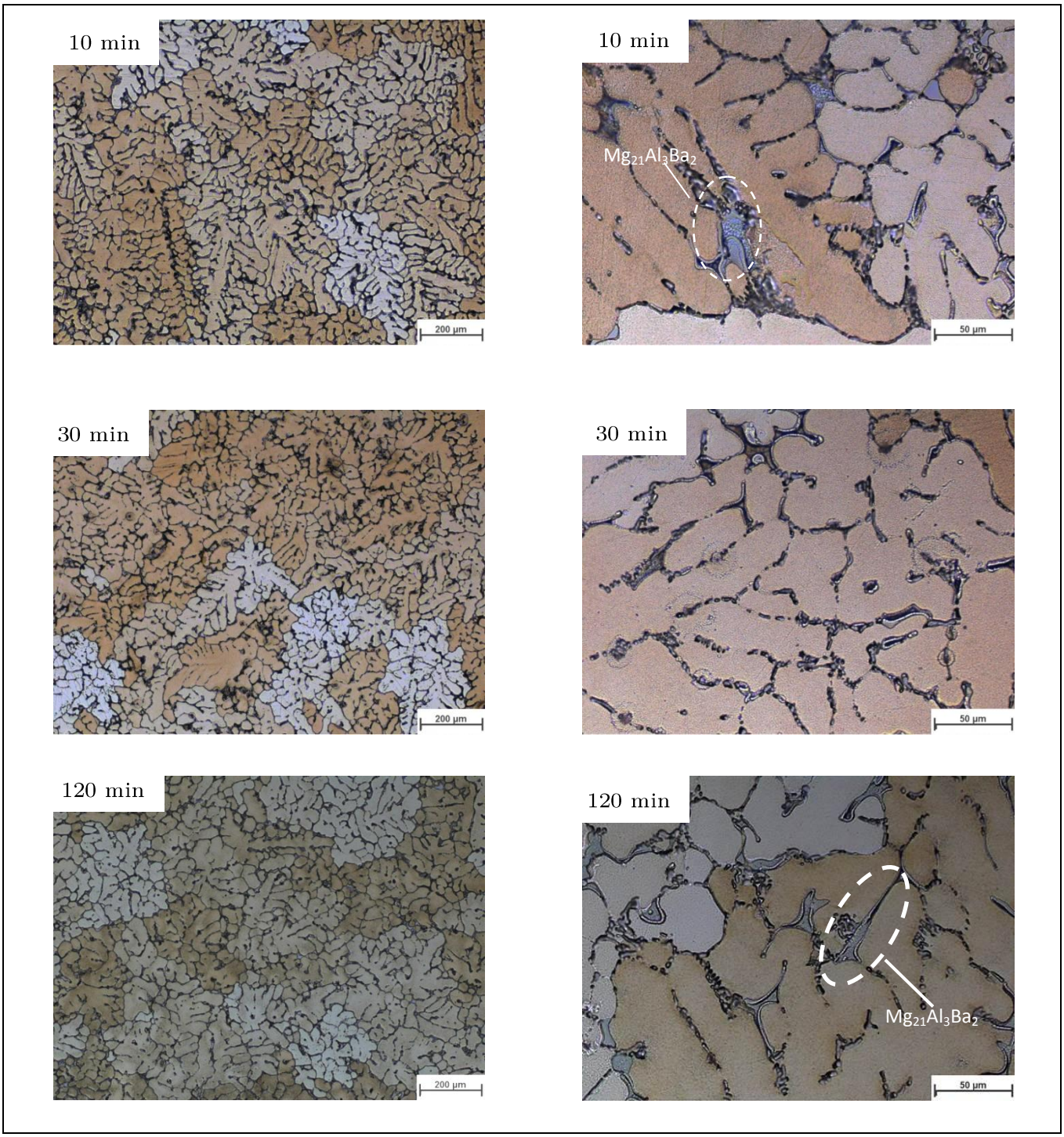

Figure 24: Ageing process at 180°C for 10, 30, 120 minutes with two magnifications

At all four ageing processes which are shown in Figure 24 the dendritic grains are surrounded by the $Mg_{21}Al_3Ba_2$ phase. Besides the $Mg_{21}Al_3Ba_2$ phase in the inter-dendritic spacing, the lamellar Al_2Ca phase was also present for all four ageing times at 180°C.

The second ageing process was implemented at ***200°C*** for 10, 30, 80, 120 and 180 minutes the resulting microstructures are shown in Figure 25. However, due to less differences in the microstructure, only micrographs for 10, 30 and 120 minutes are presented.
The dendritic microstructure of the grains and the $Mg_{21}Al_3Ba_2$ phase were preserved. According to the pores on the surface in Figure 25, they are artefacts from the polishing and etching process. As before, on the left hand side always a magnification of 100x, whereas on the right hand side a magnification of 500x was used.

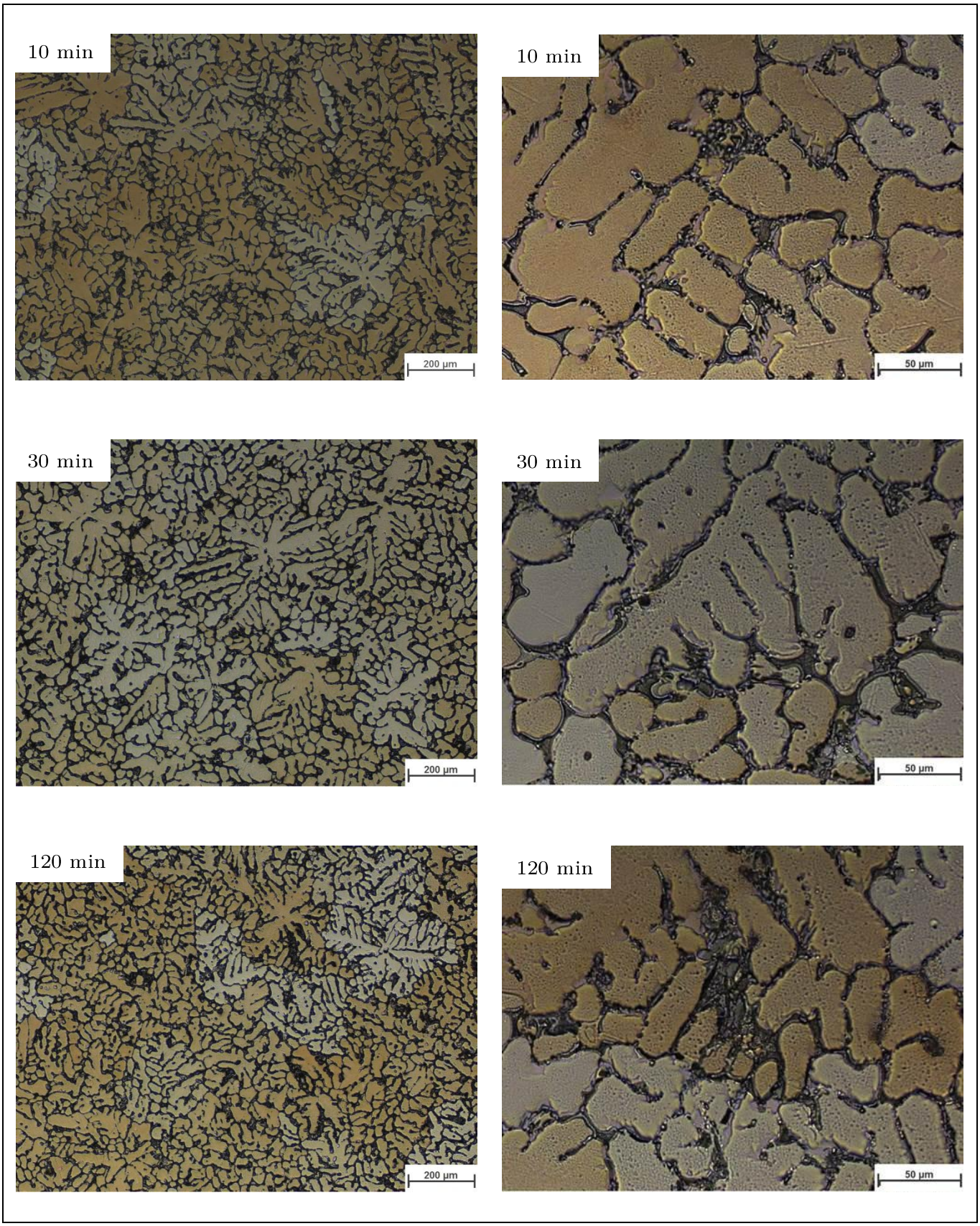

Figure 25: Ageing process at 200°C for 10, 30, 120 minutes

The third ageing process was carried out at ***250°C*** for 10, 30, 80 and 120 minutes. In Figure 26, dark spots in the sample of 30 minutes were observed. They consist of fine lamellar phases, but it was not possible to get a LOM image in detail due to the limited magnification. The dendritic microstructure was preserved for all four soaking times. The results of 80 minutes are not presented, however they are comparable to a time of 30 minutes.

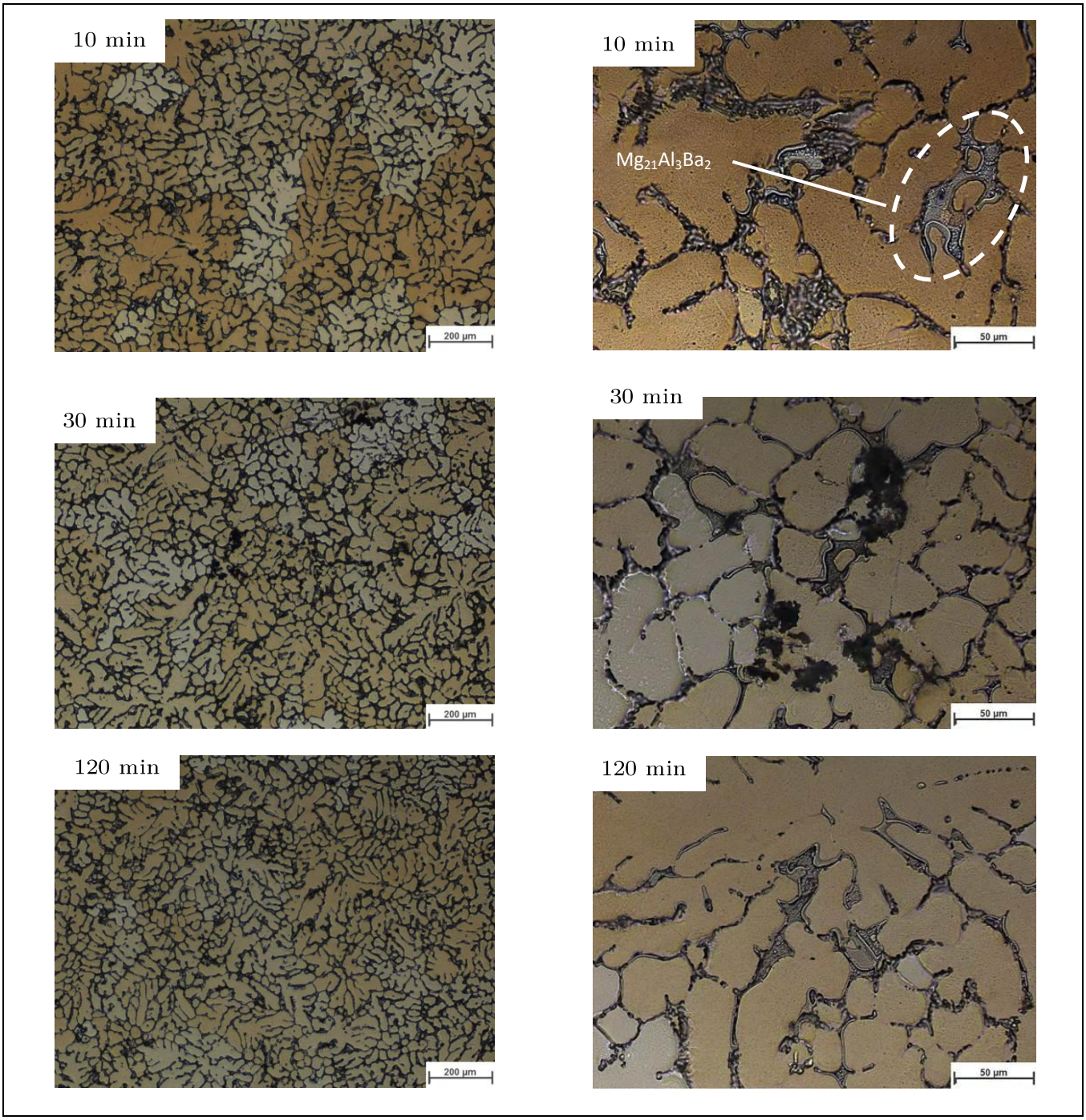

Figure 26: Ageing process at 250°C for 10, 30, 120 minutes

The fourth ageing process was implemented at ***300°C*** for 10, 30 and 120 minutes. The dendritic structure globularizes and is visible after a duration time of 120 minutes.

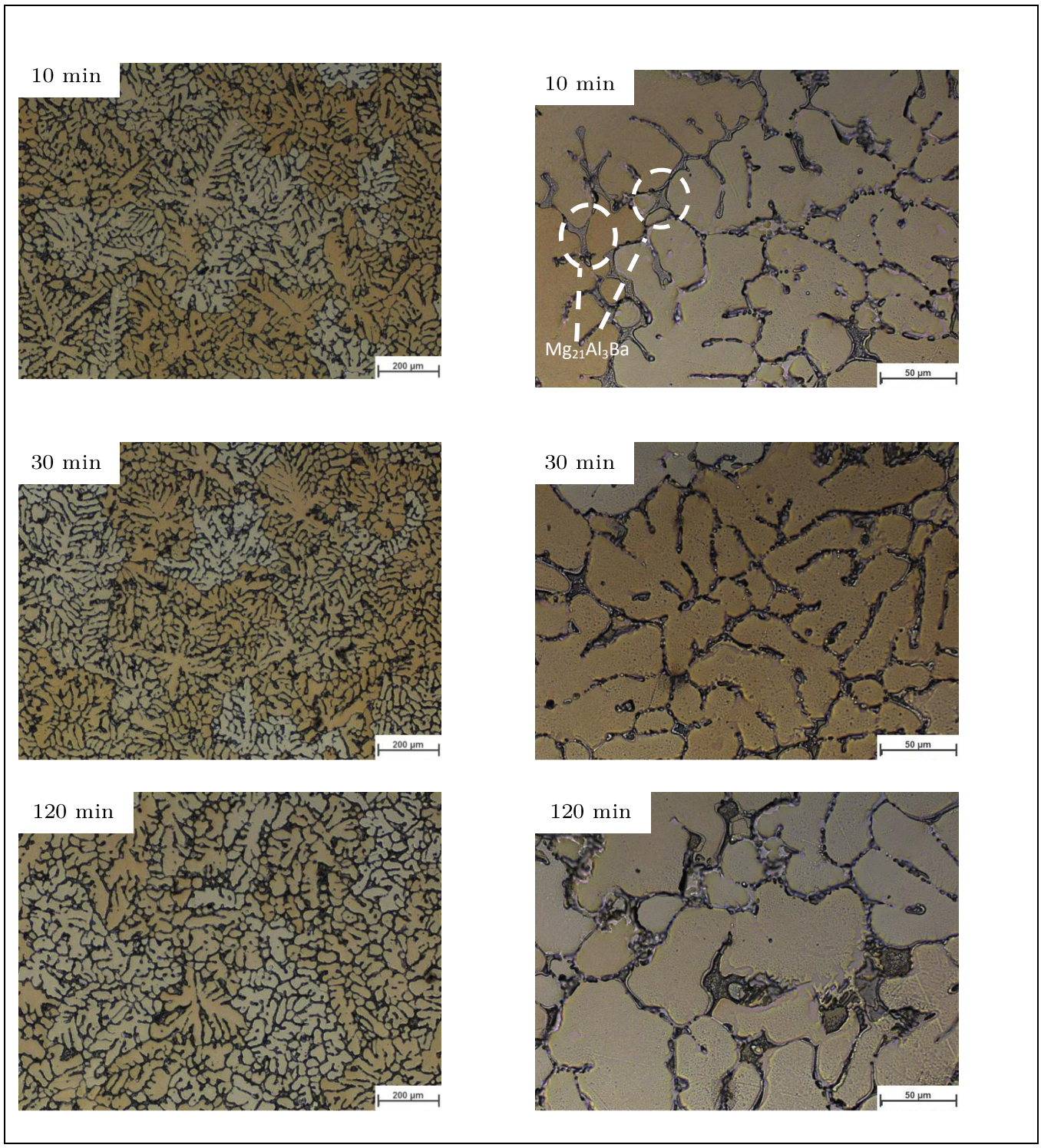

Figure 27: Ageing process at 300°C for 10, 30, 120 minutes

4.2 Hardness testing

The results of the hardness measurements are shown in Table 13 and Table 14. Table 13 shows the hardness values of the as-received state and after the homogenisation and the solution heat treatments. The hardness values of the aged samples are shown in Table 14.

Table 13: Hardness values of the as-received condition and the solution treated sample

	Temperature [°C]	Duration [min]	Mean value bright phase [HV0.05]	Mean value dark phase [HV0.05]	Mean value both phases [HV0.05]
As-received	-	-	79.3 ± 2.2	78.4 ± 2.6	78.8 ± 2.3
Homogenisation	500	1440	70.3 ± 3.4	74.5 ± 3.0	72.4 ± 3.7
Solution treatment	520	60	76.0 ± 2.9	75.5 ± 4.1	75.8 ± 3.3

Table 14: Hardness values of the ageing samples

Ageing temperature [°C]	Ageing time [min]	Mean value bright phase [HV0.05]	Mean value dark phase [HV0.05]	Mean value both phases [HV0.05]
180	10	76.20 ± 1.79	74.50 ± 4.79	75.44 ± 3.32
	30	74.75 ± 1.50	73.50 ± 1.30	74.13 ± 1.46
	80	78.60 ± 5.89	77.80 ± 3.83	78.20 ± 4.71
	120	81.80 ± 4.55	73.75 ± 2.36	78.22 ± 5.52
200	10	73.80 ± 6.02	79.40 ± 5.42	76.60 ± 6.15
	30	75.33 ± 2.08	77.67 ± 2.52	76.50 ± 2.43
	80	81.40 ± 3.04	80.00 ± 5.03	80.78 ± 3.83
	120	79.00 ± 8.18	75.67 ± 8.08	77.33 ± 7.50
	180	80.80 ± 2.28	79.50 ± 3.67	80.09 ± 3.05
250	10	73.00 ± 3.46	77.50 ± 2.38	75.57 ± 3.55
	30	82.75 ± 5.68	77.25 ± 6.34	80.00 ± 6.30
	80	76.40 ± 2.51	81.00 ± 3.67	78.70 ± 3.83
	120	76.25 ± 2.87	74.00 ± 3.00	75.26 ± 2.93
300	10	72.75 ± 8.92	73.00 ± 5.48	72.88 ± 6.85
	30	71.20 ± 3.03	60.25 ± 1.89	66.33 ± 6.27
	120	66.00 ± 3.67	60.25 ± 8.22	60.50 ± 5.24

When comparing the hardness values of the solution treated sample with the results of the ageing samples, it can be clearly seen that the hardness increased for the samples aged at 180°C, 200°C and 250°C. For the samples aged at 300°C, the hardness decreased even after short heat treatments.

Plots of mean hardness values were generated against the ageing time in order to get a better overview (see Figure 28, Figure 29, Figure 30 and Figure 31).
The hardness values of the aged samples at 180°C are shown in Figure 28. A slight increase in hardness is observed.

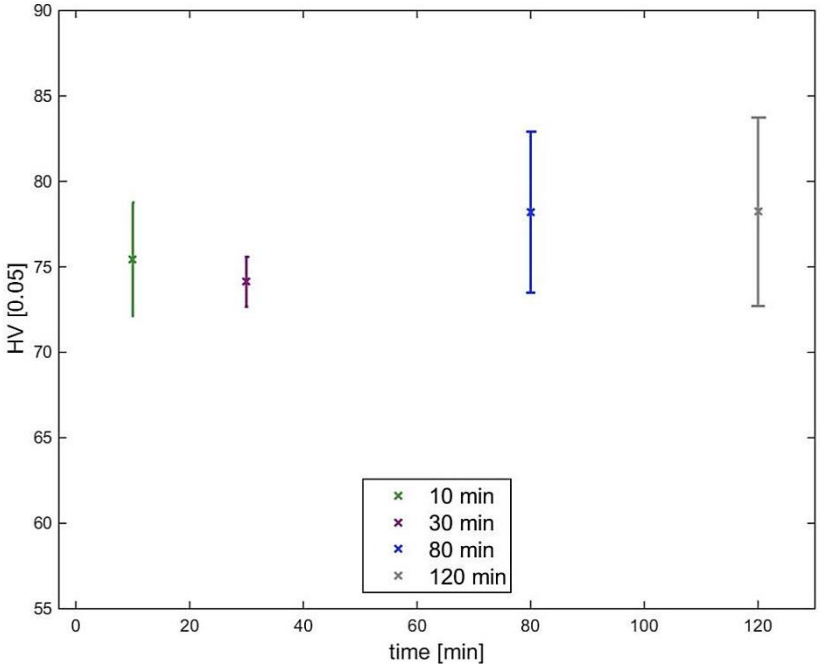

Figure 28: Overview of the hardness from the aged samples at 180°C

In Figure 29 a maximum of the hardness can be seen between 80 and 180 minutes. An additional ageing experiment performed over a period of time of 180 minutes was added.

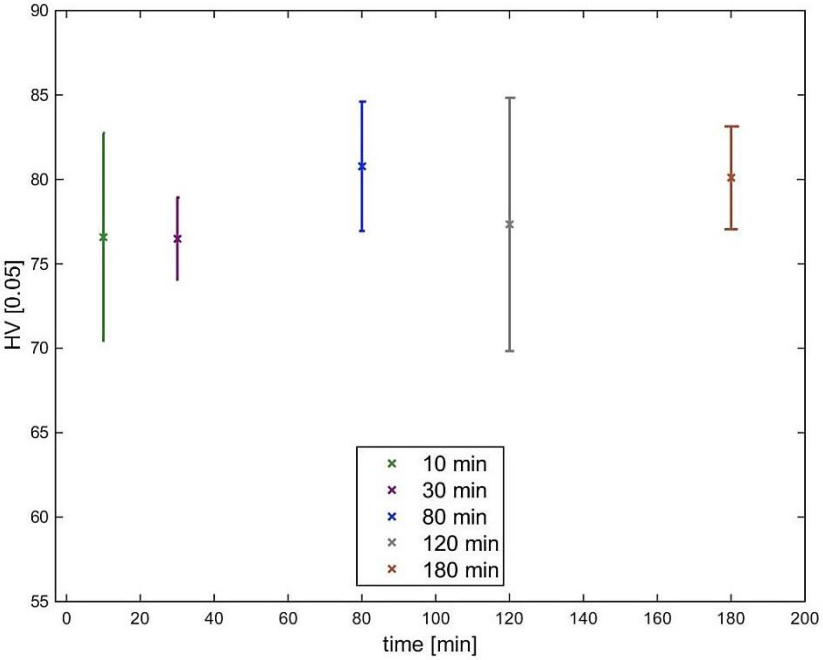

Figure 29: Overview of the hardness from the aged samples at 200°C

For the ageing temperature of 250°C the maximum hardness was reached after 30 minutes of treatment, as shown in Figure 30.

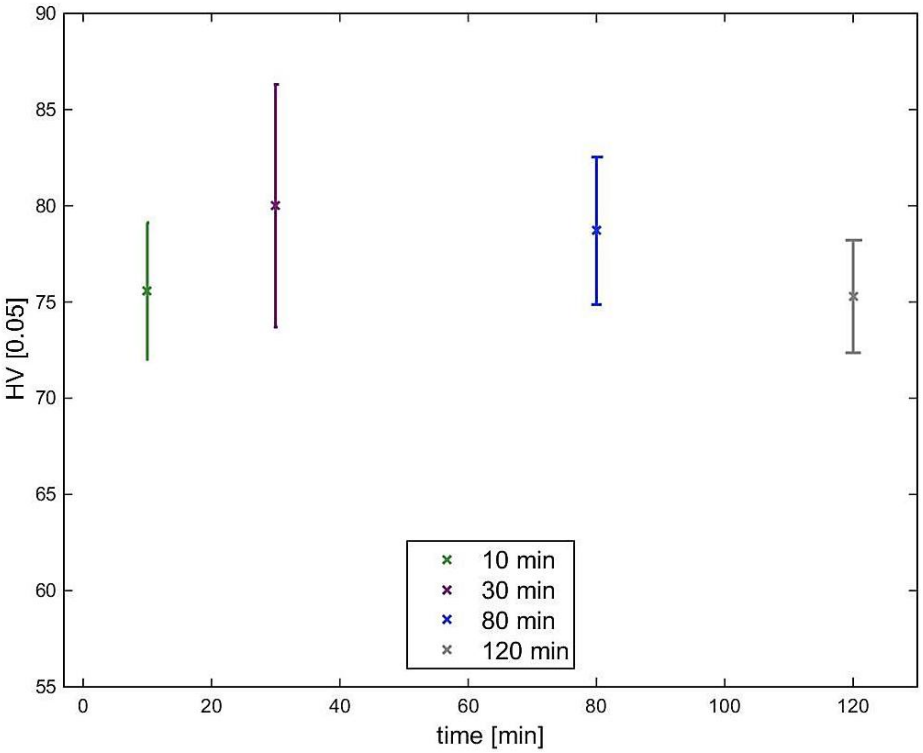

Figure 30: Overview of the hardness from the aged samples at 250°C

After treatments at 300°C (see Figure 31), the hardness decreased constantly with the ageing time.

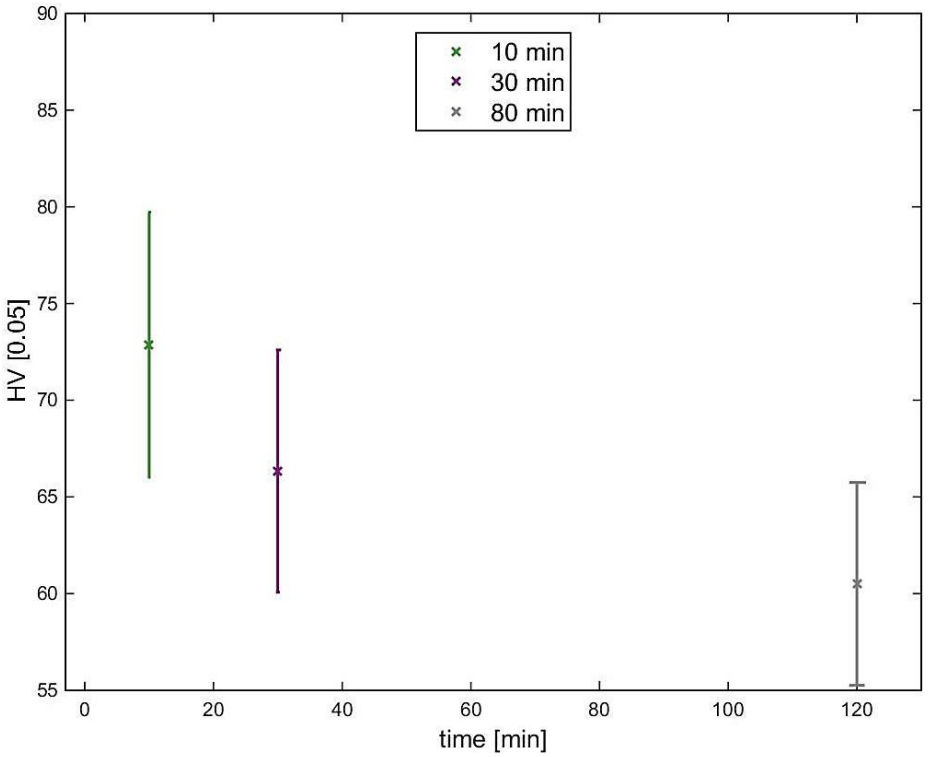

Figure 31: Overview of the hardness from the aged samples at 300°C

4.3 Differential scanning calorimetry

The as-received and the solution treated samples were measured with the Netzsch 409c device. The results from these investigations show two small peaks at the beginning of the measurement in the temperature range from 25°C-100°C (see (A) in Figure 32). They occur due to the heating process. Some sort of barrier has to be overcome in order to heat the sample homogeneously. Therefore, the temperature range from 25°C-100°C was ignored for further evaluation of the DSC measurements using Netzsch409c device.
The solution treated sample was investigated with the Netzsch 409c and the Q2000 to compare the accuracy of the devices (Figure 33 and Figure 34). The aged samples were investigated by means of the DSC Q2000 (Figure 35 to Figure 38). For the results obtained using both devices, the exothermic direction was selected downwards.

The heat flow curves obtained from the ***as-received*** condition are shown in Figure 32. The first endothermic peak (see chapter 3.6) occurs at 555°C (B) during the heating process. In this case, the peaks at 555°C and 580°C (C) were identified as melting peaks of inter-dendritic phases. B_S in Figure 32 represents the beginning of the melting. The last endothermic part of a peak in the heating process is related to the partial melt of α-Mg (D). Three exothermic peaks occur during cooling 585°C (D') where solidification of α-Mg starts, 560°C (C') and 525°C (B'). These peaks are referring to solidification processes of the α-Mg and two inter-dendritic phases, respectively.

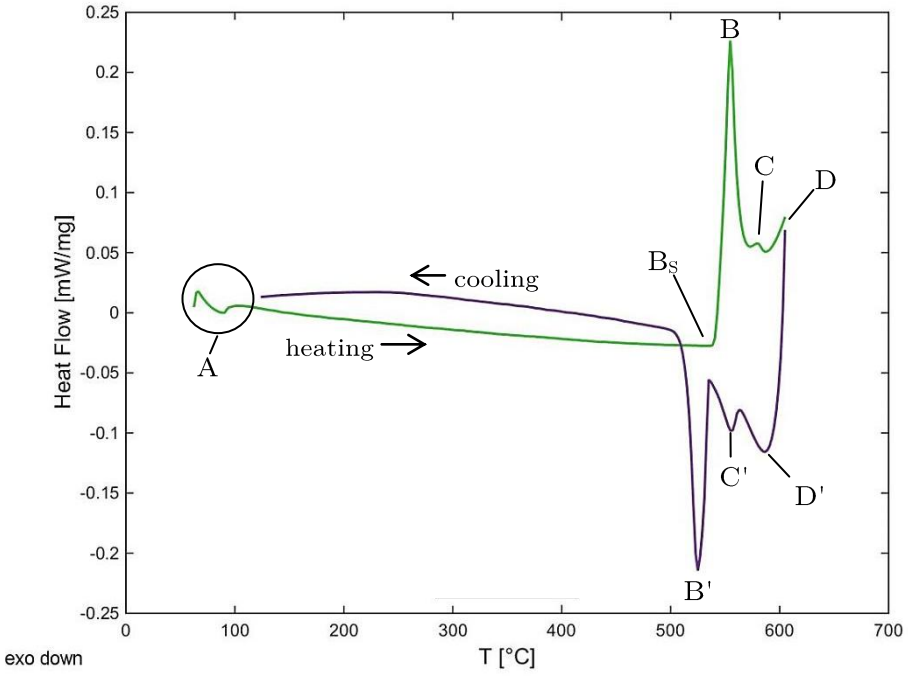

Figure 32: DSC analysis from the as-received condition

Besides the endo- and exothermic peaks which were discussed above, the ***solution treated*** sample shows additionally two exothermic peaks during the heating process (see (E) and (F) in Figure 33). The first peak in Figure 33 appears at

240°C (E) and the second at 333°C (F). Comparing Figure 33 with Figure 34 it can be seen, due to the better resolution of DSC Q2000 three peaks in Figure 34 arise at 225°C (E), 320°C (F) and 420°C (G).

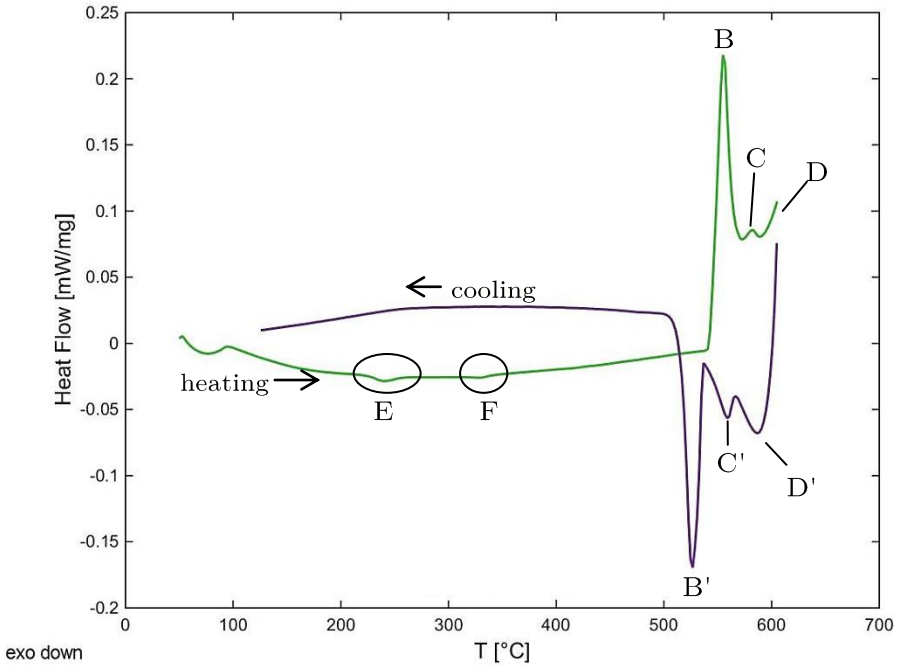

Figure 33: DSC curves (Netzsch 409c) of the solution treated sample

In Figure 34, these two additionally exothermic peaks from Figure 33, arise at 225°C (E) and 320°C (F) but they are standing for the same conversion as the peaks in Figure 33 at 240°C (E) and 333°C (F). Due to the better resolution of the Q2000, an additional exothermic peak can be seen at 408°C (G) in Figure 34.

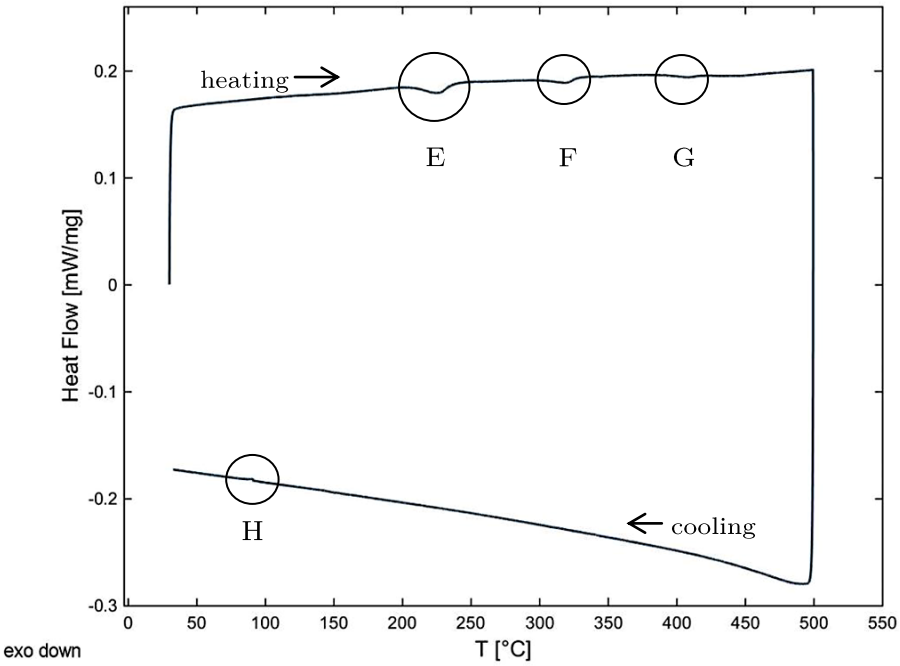

Figure 34: DSC curve (Q2000) of the solution treated sample

A further difference between Figure 33 and Figure 34 is given by a small peak at the cooling curve in the temperature range from 85°C-95°C (H).

Finally, the ***aged*** samples were investigated with the DSC, Q2000.
The sample aged at *200°C for 10 minutes* is shown in Figure 35. Two exothermic peaks at 320°C (F) and 408°C (G) can be seen during heating and a peak during cooling at 130°C (H).

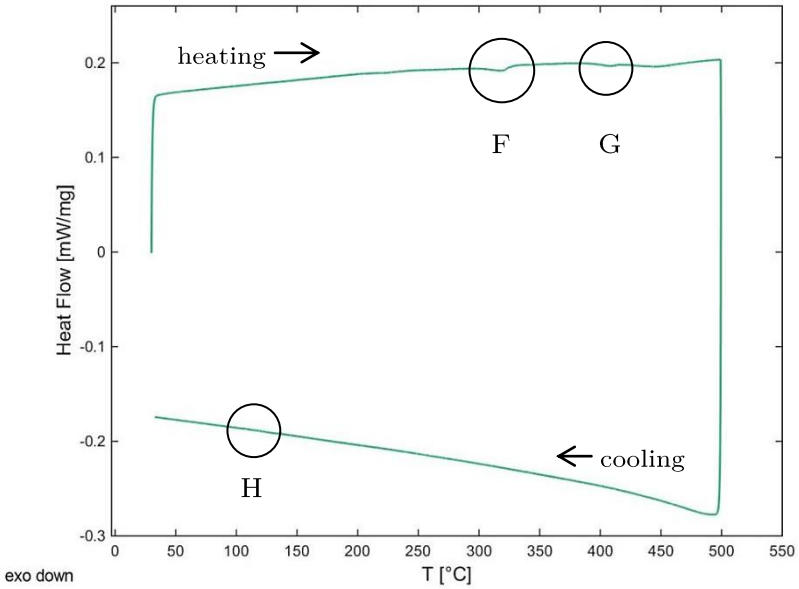

Figure 35: DSC curve; ageing process at 200°C for 10 minutes

The sample aged at *200°C for 120 minutes* (see Figure 36) shows two exothermic peaks at 320°C (F) and 408°C (G) on the heating curve and one exothermic peak at the cooling curve at 120°C (H).

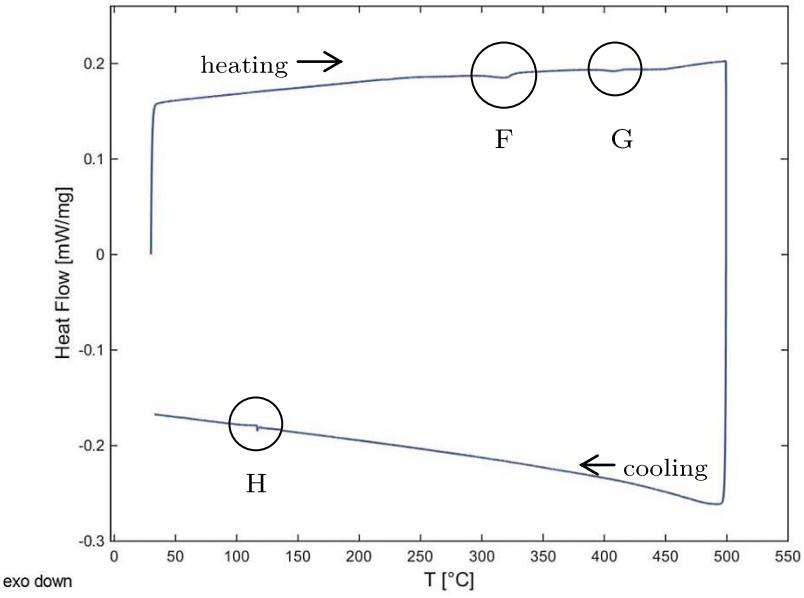

Figure 36: DSC curve; ageing process at 200°C for 120 minutes

The sample aged at *250°C for 10 minutes* shows two exothermic peaks on the heating curve at 323°C (F) and 420°C (G). Moreover, two exothermic peaks are visible at the cooling curve at 83°C (H') and 130°C (H).

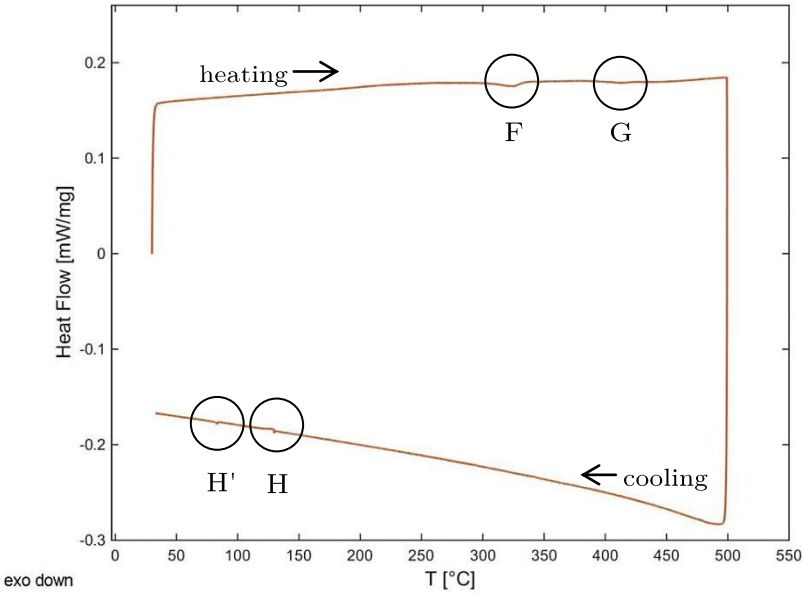

Figure 37: DSC curve; ageing process at 250°C for 10 minutes

The last examined sample was aged at *300°C for 120 minutes* (see Figure 38). The result from this investigation shows only one exothermic peak during the heating process at 408°C (G). Only one peak appears at 105°C during cooling (H).

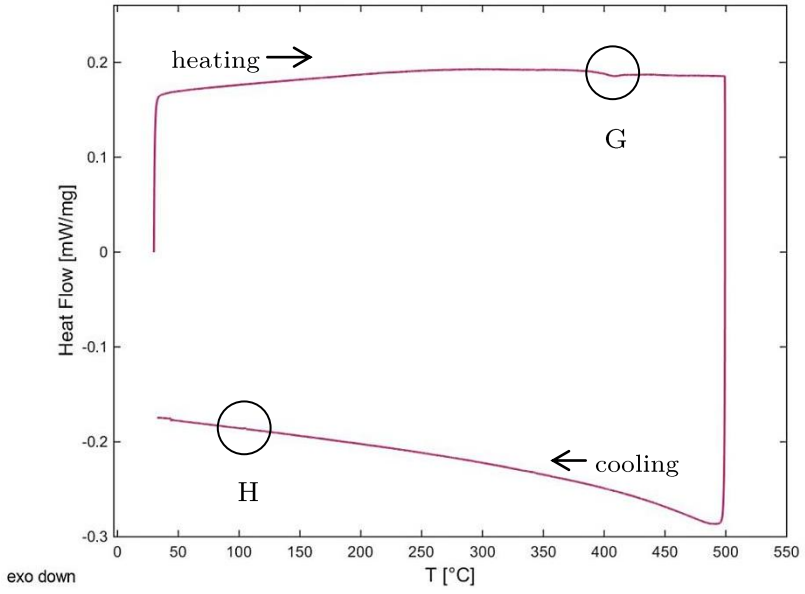

Figure 38: DSC curve; ageing process at 300°C for 120 minutes

4.4 MatCalc Simulations – Thermodynamic equilibrium

Figure 39 shows the result of the first "stepped equilibrium calculation". The resulting solidus and liquidus temperatures were in the range from 540°C to 610°C. At 610°C the α-Mg starts to solidify. The $Mg_{21}Al_3Ba_2$ phase appeared around 560°C, respectively. The $(Mg,Al)_2Ca$ phase starts to solidify at 540°C and is replaced by the Al_2Ca phase at 495°C. The $Mg_{17}Al_{12}$ phase appeared at 155°C.

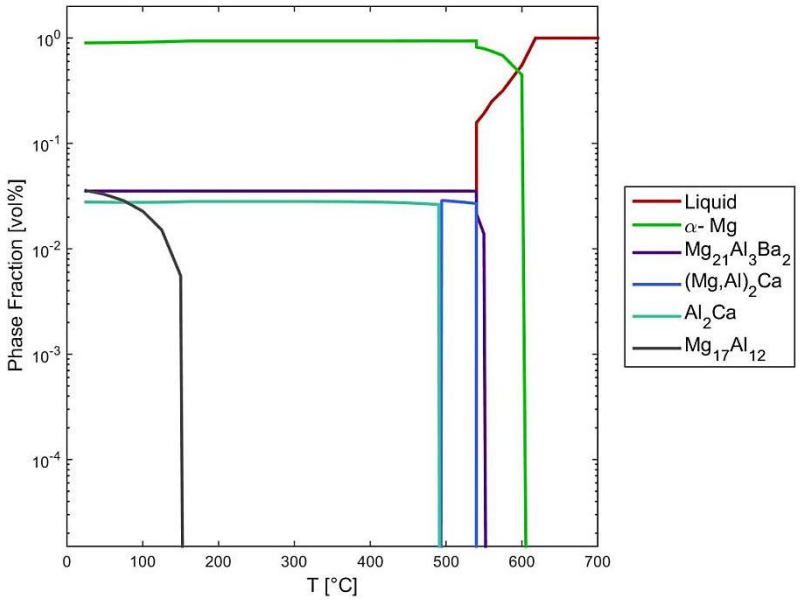

Figure 39: First equilibrium calculation

In Figure 40 the result of the second "stepped equilibrium calculation" is shown, after the simulated homogenisation heat treatment. The resulting solidus and liquidus temperatures were in the range from 570°C to 637°C, respectively. The $Mg_{21}Al_3Ba_2$ phase appeared around 520°C, followed by $(Mg,Al)_2Ca$ and Al_2Ca with their solidus temperatures at 520°C and 495°C, respectively. The $Mg_{17}Al_{12}$ phase appeared at 170°C.

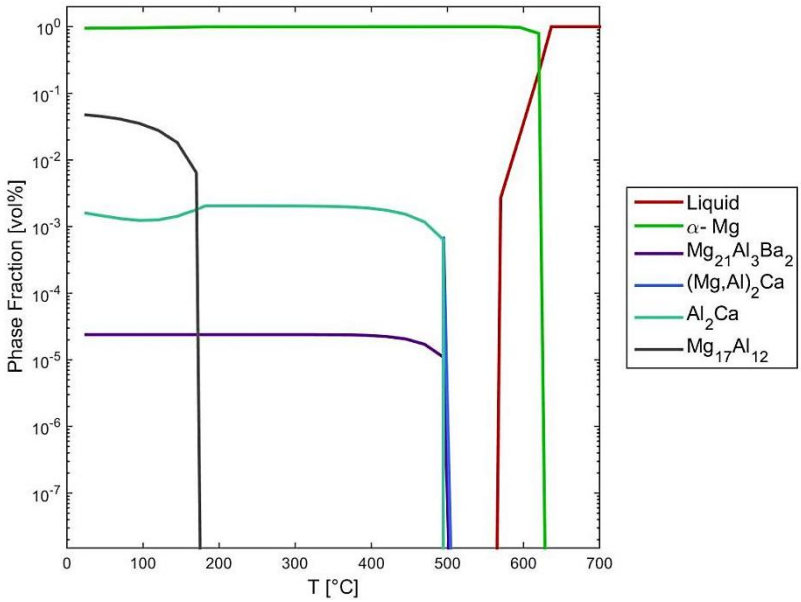

Figure 40: Second equilibrium calculation

5 Discussion

This chapter is divided into the discussion of phases in equilibrium and the discussion of precipitation kinetics.

5.1 Phases in equilibrium

The MatCalc simulation of the equilibrium state (see Figure 39) showed that the first solidified phase is α-Mg. This phase starts to solidify at 610°C and the dendrites in the microstructure consist of almost pure α-Mg, as can be seen in Figure 19, Figure 20 and Figure 23. Comparing with the DSC curve shown in Figure 32, it can be concluded that at 600°C the α-Mg phase was not completely melted during the 10 °C/min measurement.

The next solidifying phase, according to Figure 39, is the Ba-rich phase, $Mg_{21}Al_3Ba_2$, which appears at around 560°C. It is distributed almost randomly in the matrix with a few agglomerations as it is shown in Figure 20 and Figure 23.

The subsequent phase that appears in Figure 39 is the $(Mg,Al)_2Ca$ phase. It is a Laves C36 phase as explained in chapter 2.3. This phase has a hexagonal crystal structure but it transforms into the Al_2Ca phase at 495°C. The Al_2Ca phase is a Laves C15 phase, with a cubic crystal structure. Actually the two Laves phases C36 and C15 are similar in their crystal structure. The transition from the hexagonal C36 structure to the more stable cubic C15 structure should happen in a diffusionless way without nucleation and growth processes. If this is not the case, than the transformation consists of dissolution and growth of nuclei and then there must be an endo- and exothermic peak in the DSC analysis (see Figure 32) but this is not the case for ABaX422. Furthermore, Han et al. [41] implied that the Al_2Ca phase can block the grain boundary sliding due to its "step-like" shape (see Figure 41) which is good for the creep resistance. As it is shown in Figure 41, there is always a layer of Al_2Ca followed by α-Mg, alternately. Figure 41 b) shows the interpretation of the solidification process by means of DSC measurement.

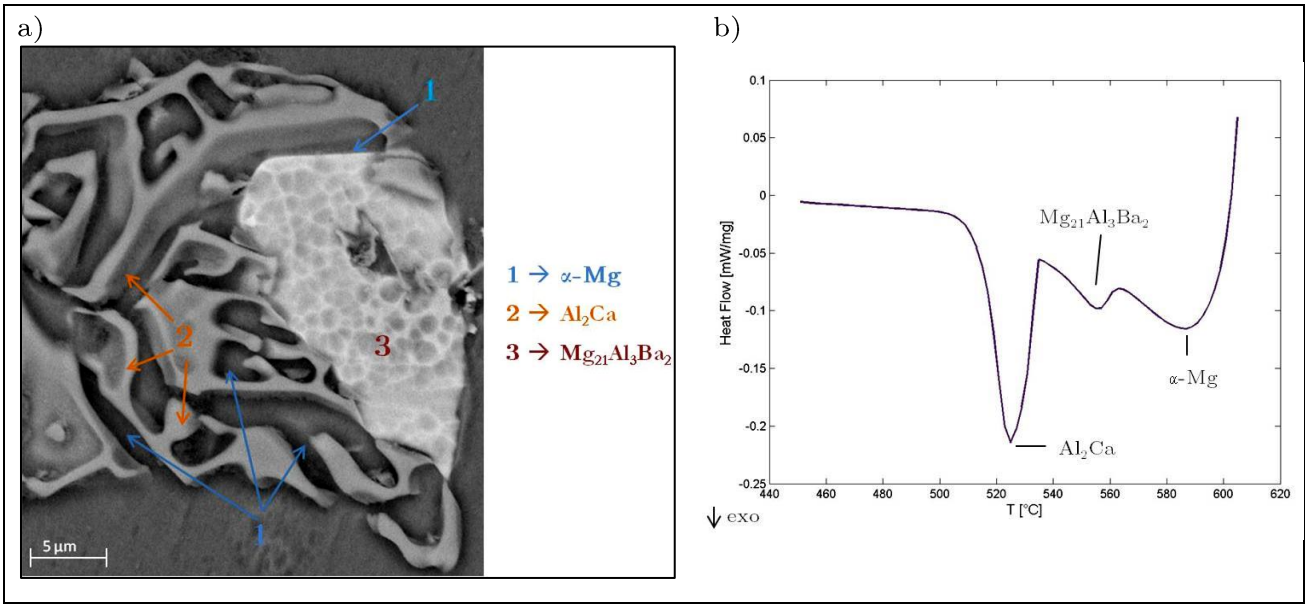

Figure 41: a) BSE image from a solution treated sample to show the alternately layers of α-Mg and Al_2Ca; b) detail of the cooling curve (DSC) showing solidification of phases

Lastly the $Mg_{17}Al_{12}$ phase appeared at 155°C. It should be taken into account, that the ABaX422 alloy is designated to be creep resistant. But, if the $Mg_{17}Al_{12}$ phase exists then the creep resistance cannot be guaranteed due to the low melting point of this phase. However, after various heat treatments (see chapter 2.5) the EDX analysis of the alloy did not show any indications that $Mg_{17}Al_{12}$ is present in ABaX422. It was also not referred in the literature that $Mg_{17}Al_{12}$ is existing in ABaX422, compare [3] and [42]. Han et al. [41] alludes to the suppression of the $Mg_{17}Al_{12}$ phase due to the formation of the $(Mg,Al)_2Ca$ phase when the content of Ca is higher than 2 wt% . The $Mg_{17}Al_{12}$ phase is present in the MatCalc simulation due to the fact that it is a new database and that the suppression of this phase is not explicitly proven for ABaX422. The small (H) exothermic peaks (Figure 33 - Figure 38), on the other hand, could be related to the appearence of this phase in the low temperature range.

To sum up, after the first equilibrium calculation three main phases remain at room temperature which are the α-Mg phase, the major constituent of the dendrites, followed by the $Mg_{21}Al_3Ba_2$ phase and the Al_2Ca phase in the inter-dendritic region.

Additionally to the first equilibrium calculation, a second equilibrium calculation was accomplished to simulate the homogenisation process (see Figure 40). The MatCalc simulation showed that the Al_2Ca phase is the second important phase after the α-Mg phase. This result was confirmed with a solution treated sample and the cooling within the oven (see Figure 16). Due to the slow cooling process, the Al_2Ca phase had enough time to precipitate in a needle shaped form, as it is shown in Figure 16 and Figure 42. The SEM and EDX analysis proved this fact (Figure 19).

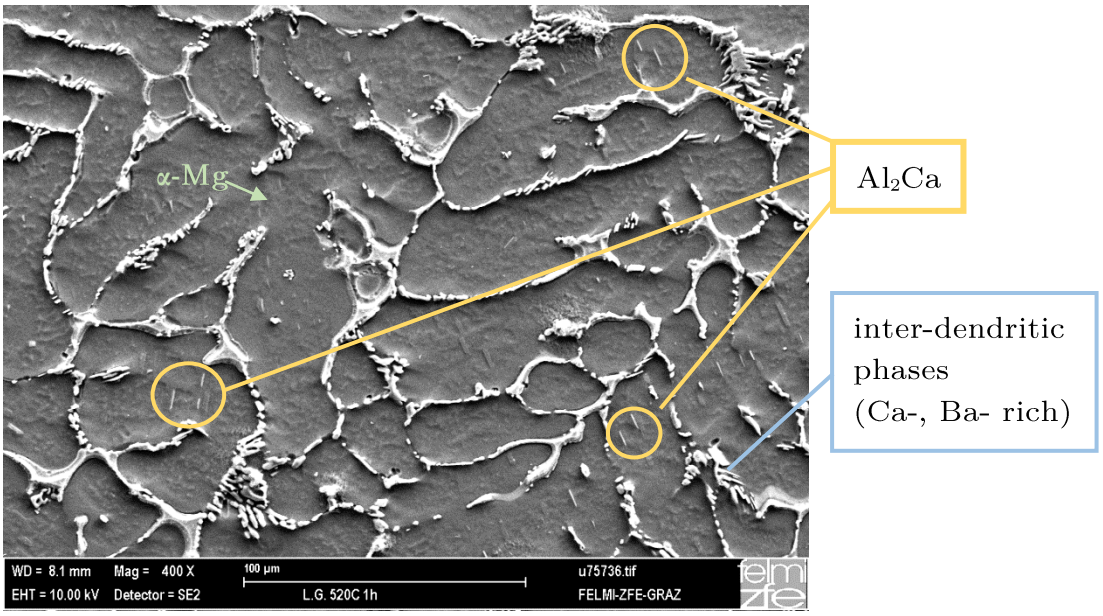

Figure 42: BSE image of the solution treated sample for 60 min at 520°C; cooling within the furnace

According to the elemental maps in Figure 20, aluminium, barium and calcium are present in the matrix because of the fast solidification process due to the water cooling after solution heat treatment.
The results of the SEM and EDX analysis confirmed the occurrence of the designated MatCalc phases in ABaX422. Additionally to these results, the thermal analysis of the samples showed three exothermic peaks on the cooling curve for samples investigated up to 600°C (Figure 32, Figure 33). The first peak appeared at 585°C, followed by one at 560°C and 525°C. Comparing the DSC curve from the as-received condition (Figure 32) with the results from MatCalc equilibrium simulations (Figure 39) the peaks were assigned to the following phases: the peak at 585°C corresponds to the α-Mg phase, the next peak at 560°C corresponds with the Ba-rich phase and the last one to the Ca-rich phase. Although, the equilibrium calculation cannot be compared one-to-one with the as-received condition due to the dynamic nature of DSC measurements, the sequency should remain the same.

5.2 Precipitation kinetics

The first step in starting a precipitation process is the removal of segregations which occurs during casting, to gain a homogeneous composition of the alloy. Therefore, the homogenisation heat treatment is performed.
The next heat treatment is the solution heat treatment to bring solutes into solid solution. Solution treatment involves heating the alloy to an adequate temperature, holding the temperature for a certain time and quenching the material. In chapter 4.1.2.2 the results of different solution treatment temperatures and soaking times are designated. Four different temperatures were chosen to find the best solution treatment temperature: 500°C, 520°C, 535°C and 550°C. Besides temperature and time, the heating rate has an additional effect on the result of the solution treatment. To the sake of scientific analysis the heating rate was chosen as fast as possible to prevent the growth of new phases during heating. Hence, a heating rate of 10 °C/s was chosen. Starting at 550°C, for all three soaking times (5, 10 and 30 minutes) the dendritic structure was replaced by a globular one and melted and re-solidified phases were occurring (see Figure 8). Similary, the treatments at 535°C also provided a globular microstructure and the melted and re-solidified phases, as can be seen in Figure 9. This is confirmed by DSC of the as-received condition (Figure 33), in which B_S at around 540°C indicates the temperature at which phases start to melt. Thus, two further temperatures were examined, 520°C and 500°C. At both temperatures the dendritic microstructure was persisting and no melted and re-solidified phases were produced. Between these two temperatures no difference was found, and so 520°C was chosen as the solution treatment temperature for a soaking time of one hour. The next point to be considered is the cooling rate of the solution treatment process. As it was mentioned above, the cooling process must be fast enough to retain all the soluble atoms in the solid solution and therefore, quenching is required. In this work two further cooling rates were investigated to

show up the influence of the cooling process on the microstructure. The samples compared to air and water quenching, cooled down to room temperature within the furnace presented needle shape precipitates in the α-Mg phase. Due to the slow cooling, diffusion took place and these precipitates were formed (Figure 16). These precipitates were examined with the LOM and as well with the SEM and EDX (see Figure 17). The BSE image (Figure 18) showed the material contrast to the α-Mg dendritic phase and the EDX analysis confirmed the assumption that these precipitates consist of aluminium and calcium (Figure 19, Position 4). The high amount of magnesium in the EDX scan from Position 4 in Figure 19 may appear due to the penetration depth of 1 µm at 10 kV energy of the electron beam.

Besides microstructural investigations, a thermal analysis was performed (Figure 33 and Figure 34). The solution treated sample was examined twice, with the Netzsch 409c and the Q2000 from TA-Instruments, due to the better resolution of the Q2000 at lower temperatures up to 500°C. At both DSC curves two exothermic peaks occurred in the temperature range from 220°C-340°C. In addition to the two exothermic peaks on the heating curve in Figure 33 there are two endothermic peaks and three exothermic peaks on the cooling curve visible. The first endothermic peak at 555°C is referred to the Ca-rich phase and the second endothermic peak at 580°C to the Ba-rich phase while comparing the results from the MatCalc simulation (Figure 39) with the DSC analysis from the as-received sample (Figure 32). Similarly to the as-received sample, melting of α-Mg starts at (D') and is not completely finished. When cooling down the sample, the α-Mg phase starts to solidify at 585°C, followed by the exothermic Ba-rich peak at 560°C (C'). The last solidifying phase is the Ca-rich phase with the corresponding exothermic peak at 525°C (D').

Solution treatment result in a hardness of 75.8 [HV 0.05] due to solid solution strengthening. To gain an increase in hardness and strength by precipitation hardening, an additional heat treatment was performed afterwards. These ageing treatments were performed at 180°C, 200°C, 250°C and 300°C for 10, 30, 80 and 120 minutes. The hardness increased compared to the solution treated state of the sample. A slight increase in hardness is observable on three of the four ageing temperatures (Figure 43). The aged sample at 250°C showed a maximum hardness reached after 60 minutes of ageing. On the other hand, the aged sample at 300°C was immediately in the overaged zone as observed from the decrement in hardness.

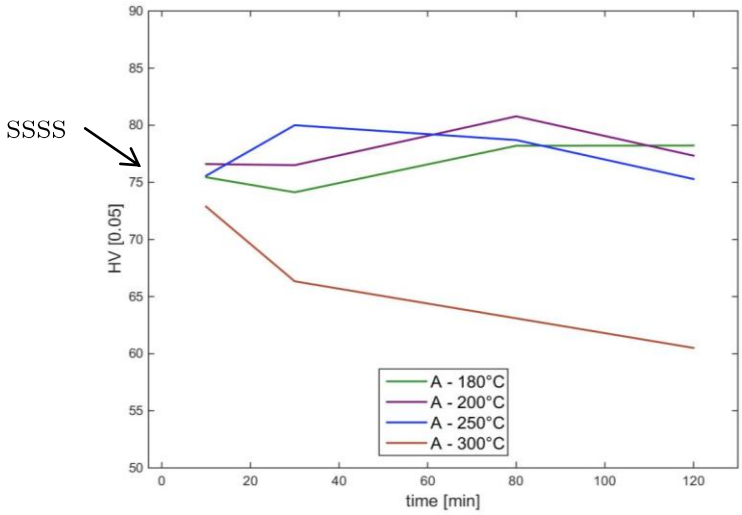

Figure 43: Hardness of ABaX422 after ageing

The summary of DSC curved during heating performed with the Q2000 are shown in Figure 44. These curves allow to determine which phases are already formed during every treatment since they will not produce a exothermic peak during heating. The solution treated sample showed three exothermic peaks (E, F, G). The first exothermic peak at 220°C is not observable at any of the other DSC curves, corresponding to the aged samples. When comparing all four ageing DSC curves it can be seen that there are two exothermic peaks (F and G). The last DSC curve corresponding to a treatment of 300°C for 120 minutes shows one exothermic peak (G). Actually, this is the same sample condition which is immediately in the overaged zone, regarding the hardness measurements (Figure 31). Due to this, it can be concluded that the exothermic peak (F) at 320°C represents the precipitation of a stable phase that do not contribute to hardness. Finally, the phase formed at around 230 °C (E) (see Figure 44) is the metastable hardening phase that is formed from the solid solution state, is still not completely formed after a treatment at 200°C for 10 minutes, and was completely precipitated at higher temperatures and longer temperatures during ageing processes.

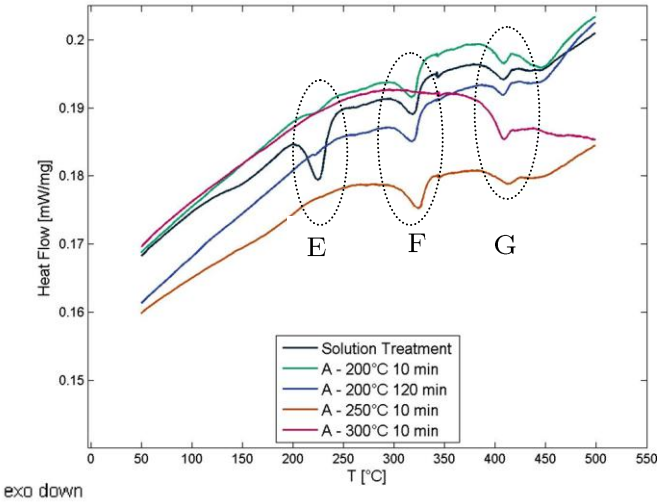

Figure 44: DSC curves (heating) from elevated ageing samples (Q 2000 device)

6 Summary and Conclusions

In the present thesis heat treatments were applied with the objective to understand precipitation kinetics of phases that improved the hardness and that may have a positive effect in the creep resistance of this alloy.

The microstructure of the ABaX422 alloy was characterized by means of LOM. Furthermore, microhardness measurements and thermal analysis were carried out for samples in the as-received condition and after homogenisation, solution treatment and ageing. To gain information over the present phases, thermodynamic equilibrium simulations were performed with MatCalc, as shown in Figure 39. The alloy consists of three main phases: α-Mg within the dendrites, Ba-rich ($Mg_{21}Al_3Ba_2$) and Ca-rich (Al_2Ca) phases in the inter-dendritic spacing. Hence, the Al_2Ca phase tends to form a lamellar phase in the inter-dendritic spacing as it is shown in Figure 22.
The segregations which occur during casting were removed with a homogenisation heat treatment of 24 hours at 500°C. The solution heat treatment was carried out for 1 hour at 520°C. Three different cooling rates were tested: free cooling in air, water quenching, cooling within the furnace. Water quenching was performed to hold the solutes in solution and to gain solid solution hardening. The cooling process within the furnace showed, that Al_2Ca precipitates tend to form needle shaped in the dendritic structure (Figure 16).
Ageing treatments were carried out at 180°C, 200°C, 250°C and 300°C.
A metastable phase was examined during DSC analysis (Figure 44) of aged samples. The peak (F) at 250°C is responsible for the hardening observed during ageing at 200°C for 2 hours. Peak (G) at 320 °C in Figure 44 represents a stable phase which is not occuring during ageing at 300°C, due to overageing. The hardness increment (Figure 43) is slight and as a matter of fact, creep and tensile tests are needed.

7 Outlook

Due to the ongoing weight reduction of products in the automotive and aerospace industry, further investigations will help to better understand the precipitation kinetics in the ABaX422 alloy and its improvement of the creep resistance.

I suggest some specific future topics:

- The appearance of the $Mg_{17}Al_{12}$ phase and metastable phases should be analysed using data of wide and/or small angle X-ray scattering (WAXS and SAXS) measurements, obtained already at Elettra under the proposal number: 20145397.

- TEM investigations of the precipitates should be done to get information on their lattice structure. It can also be possible that these precipitates are the $(Mg,Al)_2Ca$ phase which has a different lattice structure than Al_2Ca.

- Further examination of the exo- and endothermic peaks which occur during the cooling process of the DSC measurements must be done. Figure 45 shows an excerpt of the cooling curves of the above discussed samples. Are these peaks related to $Mg_{17}Al_{12}$ formation, or to any other process?

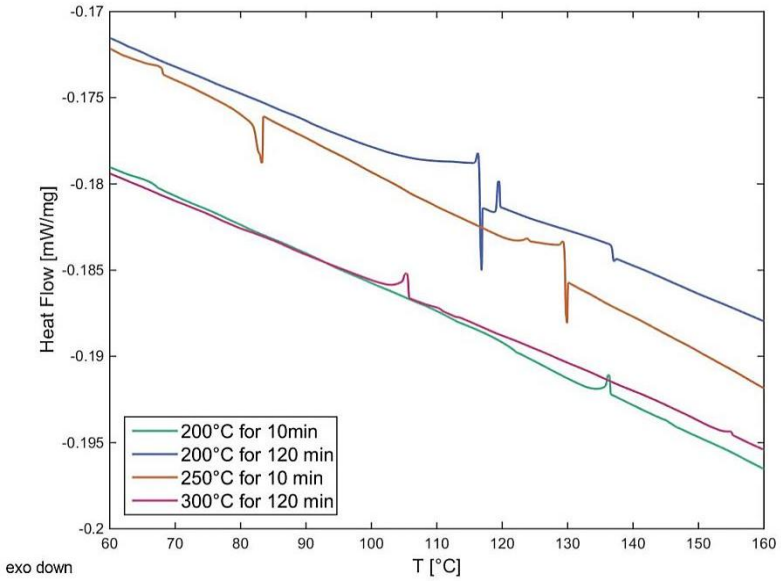

Figure 45: DSC curves; excerpt of the cooling curves from Figure 35, Figure 36, Figure 37, Figure 38

- Creep investigations of the alloy should be carried out after the proposed heat treatment.

7.1 Synchrotron experiments

In order to study the precipitation kinetics more precisely, synchrotron measurements have been performed based on first results of this thesis. The synchrotron measurements were carried out at "Elettra-Sincrotrone Trieste" [43] in June 2015.
The results of this thesis were used to plan the measurements using SAXS and WAXS. According to the SAXS measurements, a larger sample volume, giving more statistical information can be examined. Investigations using conventional methods such as in-situ measurements like DSC and dilatometer present only a partial view of the complete picture in the study of precipitation kinetics. With DSC measurements no isothermal treatment can be performed. The high energy and the brilliance of the X-rays give a better resolution as X-rays used in general laboratories. The combination of SAXS with WAXS allows the characterisation of the type of precipitates in the early stages.
The synchrotron measurements were carried out for as-cast, extruded and deformed samples. In order to investigate the precipitation kinetics two different heating rates and holding times were applied, depending on the experiment. Four different temperatures were used regarding the ageing temperatures. The ageing processes of the samples were investigated in-situ at the SAXS beamline.
Due to still on-going evaluation of the received data, only preliminary results are shown in Figure 46 concerning to WAXS investigations of as-received and solution treated state. The curves in Figure 46 (begin and end) correspond to the heating process which was carried out during the WAXS measurements. The first measurement (green line) was carried out at room temperature. Then the samples were heated up to 300°C (grey line).

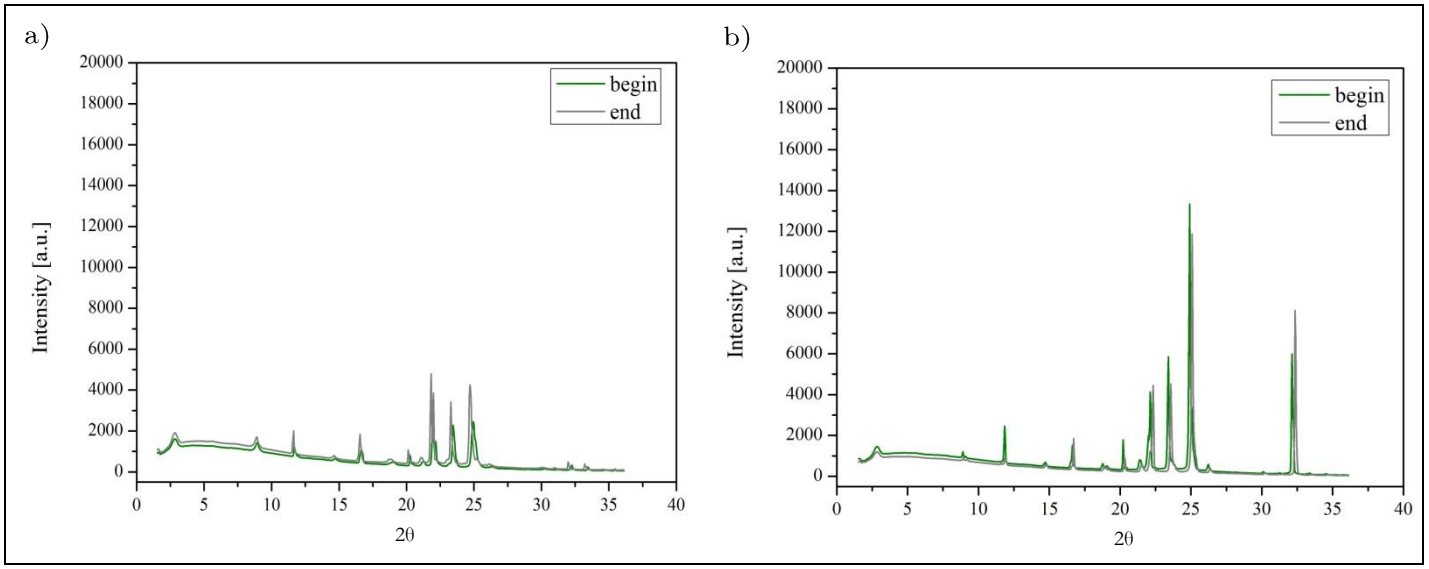

Figure 46: WAXS results from a) as-received and b) solution treated sample before (green line) and after heating up to 300°C (grey line)

8 List of Figures

Figure 1: Excerpt of the Mg-Al binary phase diagram [15] 4
Figure 2: Mg-Ca binary phase diagram [16] 4
Figure 3: The three different types of Laves phases [17] 5
Figure 4: Sketch of the heat treatment cycle consisting of homogenisation (500°C, 24 hours), solution treatment (520°C, 1 hour) and different ageing processes; Number 1 indicates free cooling, 2 indicates a heating rate of 10 °C/s, 3 represents quenching with helium 12
Figure 5: Specification of the bright and dark phases for hardness measurements; sample condition: ageing at 250°C for 80 min 14
Figure 6: a) and b) Material in the as-received condition; c) Z-stacking image of as-received condition 18
Figure 7: a) Material after homogenisation heat treatment; b) Z-stacking image of as-received condition 19
Figure 8: Solution treatment at 550°C for 30 min 20
Figure 9: Solution treatment at 535°C for 30 min 20
Figure 10: Solution treatment at 520°C for 60 min; marked area for zoom (see Figure 12) 20
Figure 11: Solution treatment at 500°C for 60 min 20
Figure 13: Solution treatment for 60 min at 520°C; free cooling in air; marked area for zoom (see Figure 14) 21
Figure 14: Zoom of marked area in Figure 13 21
Figure 12: Marked area from Figure 10; Z-stacking mode 21
Figure 15: Solution treatment for 60 min at 520°C; cooling in the furnace 22
Figure 16: New needle shaped precipitates after a solution treatment at 520°C for 60 min; cooling in the furnace 22
Figure 17: Solution treatment for 60 min at 520°C, cooling within the furnace; SE image 22
Figure 18: Solution treatment for 60 min at 520°C, cooling within the furnace; BSE image 22
Figure 19: BSE image; solution treated for 60 min at 520°C and EDX scans from the marked positions; x-axis: energy [keV], y-axis: intensity [a.u.] 24
Figure 20: EDX mapping and BSE image from the solution treated sample (for 60 min at 520°C) 25
Figure 21: Solution treated sample for 30 min at 550°C; SE image 26
Figure 22: Solution treated sample for 30 min at 550°C; BSE image 26
Figure 23: EDX scan from the solution treated sample (550°C for 30 min); BSE image and EDX scans from 1 and 2; x-axis: energy [keV], y-axis: intensity [a.u.] 27
Figure 24: Ageing process at 180°C for 10, 30, 120 minutes with two magnifications 29
Figure 25: Ageing process at 200°C for 10, 30, 120 minutes 31
Figure 26: Ageing process at 250°C for 10, 30, 120 minutes 32

Figure 27: Ageing process at 300°C for 10, 30, 120 minutes 33
Figure 28: Overview of the hardness from the aged samples at 180°C 35
Figure 29: Overview of the hardness from the aged samples at 200°C 35
Figure 30: Overview of the hardness from the aged samples at 250°C 36
Figure 31: Overview of the hardness from the aged samples at 300°C 36
Figure 32: DSC analysis from the as-received condition.....37
Figure 33: DSC curves (Netzsch 409c) of the solution treated sample.....38
Figure 34: DSC curve (Q2000) of the solution treated sample.....38
Figure 35: DSC curve; ageing process at 200°C for 10 minutes 39
Figure 36: DSC curve; ageing process at 200°C for 120 minutes.....39
Figure 37: DSC curve; ageing process at 250°C for 10 minutes 40
Figure 38: DSC curve; ageing process at 300°C for 120 minutes.....40
Figure 39: First equilibrium calculation 41
Figure 40: Second equilibrium calculation 41
Figure 41: a) BSE image from a solution treated sample to show the alternately layers of a-Mg and Al2Ca; b) detail of the cooling curve (DSC) showing solidification of phases 42
Figure 42: BSE image of the solution treated sample for 60 min at 520°C; cooling within the furnace.....43
Figure 43: Hardness of ABaX422 after ageing.....46
Figure 44: DSC curves (heating) from elevated ageing samples (Q 2000 device)..46
Figure 45: DSC curves; excerpt of the cooling curves from Figure 35, Figure 36, Figure 37, Figure 38 48
Figure 46: WAXS results from a) as-received and b) solution treated sample before (green line) and after heating up to 300°C (grey line).....49

9 List of Tables

Table 1: Alloying elements; Designation after ASTM [4] ---- 3
Table 2: Some automotive components made of magnesium alloys [27] ---- 8
Table 3: Composition in weight percent ABaX422 [3, 34] ---- 10
Table 4: Steps for grinding and polishing ---- 11
Table 5: Composition of the etchant ---- 11
Table 6: List of heat treatments ---- 13
Table 7: Connectivity between phase transition and peak direction [38] ---- 15
Table 8: Composition in weight percent for the thermodynamic equilibrium calculation ---- 16
Table 9: Phases considered for equilibrium calculations and their MatCalc designation ---- 16
Table 10: Composition of a-Mg in weight percent after the equilibrium calculation at 500°C ---- 16
Table 11: Temperature and time of various solution treatments within the furnace ---- 19
Table 12: Summary of the different solution treatments ---- 28
Table 13: Hardness values of the as-received condition and the solution treated sample ---- 34
Table 14: Hardness values of the ageing samples ---- 34

10 Bibliography

1. A. A. Luo, M. O. Pekguleryuz, K. U. Kainer, and A. A. Kaya: '8 - Applications: aerospace, automotive and other structural applications of magnesium', in 'Fundamentals of Magnesium Alloy Metallurgy', 266-316; 2013, Woodhead Publishing.
2. B. Powell, V. Rezhets, M. Balogh, and R. Waldo, *JOM*, 2002, 54(8), 34-38.
3. H. Dieringa, Y. Huang, P. Wittke, M. Klein, F. Walther, M. Dikovits, and C. Poletti, *Materials Science and Engineering: A*, 2013, 585(0), 430-438.
4. N. Hort. 'Moderne Werkstoffentwicklungen - Magnesium', [viewed 2014 24.10.]; Available from: ftp://ftp.hzg.de/pub/hort/Hort/Moderne%20Werkstoffentwicklungen/Moderne%20Werkstoffentwicklungen-Magnesium_handouts.pdf.
5. Anon. 'International Magnesium Association', [viewed 2014 24.10.]; Available from: www.intlmag.org.
6. B. Kondori and R. Mahmudi, *Materials Science and Engineering: A*, 2010, 527(7–8), 2014-2021.
7. H. Xie, L. Jia, J. Zhang, Z. Wang, and Z. Lü, *Rare Metal Materials and Engineering*, 2012, 41(6), 958-961.
8. L. Han, H. Hu, and D. O. Northwood, *Materials Letters*, 2008, 62(3), 381-384.
9. H. Watanabe, M. Yamaguchi, Y. Takigawa, and K. Higashi, *Materials Science and Engineering: A*, 2007, 454â“455(0), 384-388.
10. R. Rausch. 'Das Periodensystem der Elemente online - Magnesium', 2010-2015 [viewed 2015 02.07.]; Available from: http://www.periodensystem-online.de/index.php?el=12&id=modify.
11. R. Rausch. 'Das Periodensystem der Elemente online - Aluminium', 2010-2015 [viewed 2015 29.07.]; Available from: http://www.periodensystem-online.de/index.php?el=13&id=modify.
12. A. Höfler. 'ahoefler.de', [viewed 2015 29.07.]; Available from: http://www.ahoefler.de/werkstoffkunde/verformbarkeit_gitterstrukturen/verformbarkeit_gitterstrukturen.php#3.2.3.
13. S. W. Xu, K. Oh-ishi, S. Kamado, F. Uchida, T. Homma, and K. Hono, *Scripta Materialia*, 2011, 65(3), 269-272.
14. P. D. G. Gottstein: 'Physikalische Grundlagen der Materialkunde'; 2007, Springer.
15. magnesium.com. 'Magnesium-Aluminium Alloys', [viewed 2015 19.08.]; Available from: http://www.magnesium.com/w3/data-bank/print.php?mgw=7&magnesium=83.
16. Anon. 'Himikatus.ru', [viewed 2015 19.08.]; Available from: http://www.himikatus.ru/art/phase-diagr1/Ca-Mg.php.
17. F. Stein, M. Palm, and G. Sauthoff, *Intermetallics*, 2004, 12(7–9), 713-720.

18. K. t. M. AG. 'Mey to Metals Die weltweit umfangreichste Werkstoffdatenbank',[viewed 2015 03.08.]; Available from: http://www.totalmateria.com/page.aspx?ID=CheckArticle&LN=DE&site=kts&NM=266.

19. C. A. P. D. Poletti, *Plasticity, Forming and Moulding Processes*, I. o. M. S. a. Welding, Editor. 2013.
20. K. t. M. AG. 'Practical Heat Treatment of Magnesium Alloys', sept. 2006 [viewed 2014 26.8.]; Available from: http://www.keytometals.com/page.aspx?ID=CheckArticle&site=ktn&NM=155.
21. K. t. M. AG. 'Heat treating of Magnesium alloys', Feb. 2004 [viewed 2014 26.8.]; Available from: http://www.keytometals.com/page.aspx?ID=CheckArticle&site=ktn&NM=93.
22. L. A. Dobrzanski, T. Transki, L. Cizek, and J. Madjeski, *Selection of heat treatment condition of the Mg-Al-Zn alloys*, in *Journal of Achievements in Materials and Manufacturing Engineering*. 2009.
23. J. F. Nie, *Metallurgical and Materials Transactions A: Physical Metallurgy and Materials Science*, 2012, 43(11), 3891-3939.
24. L. Han, D. O. Northwood, X. Nie, and H. Hu, *Materials Science and Engineering: A*, 2009, 512(1–2), 58-66.
25. I. M. Association. 'International Magnesium Association', [viewed; Available from: http://www.intlmag.org/index.cfm.
26. K. t. M. AG. 'Magnesium Alloy Castings', 2003 [viewed; Available from: http://www.totalmateria.com/Article78.htm.
27. A. A. Luo, A. K. Sachdev, C. Bettles, and M. Barnett: '12 - Applications of magnesium alloys in automotive engineering', in 'Advances in Wrought Magnesium Alloys', 393-426; 2012, Woodhead Publishing.
28. M. O. Pekguleryuz, C. Bettles, and M. Barnett: '1 - Current developments in wrought magnesium alloys', in 'Advances in Wrought Magnesium Alloys', 3-62; 2012, Woodhead Publishing.
29. F. Islam. 'Thermodynamic Modelling of Mg-Al-Ca System', [viewed 2015 19.08.]; Master's Thesis]. Available from: http://spectrum.library.concordia.ca/8175/1/MQ94726.pdf.
30. E. Kozeschnik, ed. *Thermodynamic and kinetic simulations with MatCalc - Lecture notes*, 2008.
31. I. f. W. u. Werkstofftechnologie. 'MatCalc', [viewed; Available from: http://matcalc.tuwien.ac.at/.
32. I. f. W. u. Werkstofftechnologie. 'MatCalc', [viewed 2015 6. May]; Available from: http://matcalc.tuwien.ac.at/.
33. Thermo-Calc. 'TCMG4 - TCS Mg-based alloy Database, Version 4.0', [viewed 2015 19.08.]; Available from: http://www.thermocalc.com/media/19850/dbd_tcmg4_extendedinfo.pdf.

34. M. Klein, F. Kuhlmann, P. Wittke, H. Dieringa, and F. Walther, *Materials and Corrosion*, 2014, n/a-n/a.
35. T. O. S. University. 'Center for electron microscopy and analysis', [viewed 2015 17.3.]; Available from: https://cemas.osu.edu/instrumentation/fei-quanta-200-sem.
36. FELMI-ZFE. 'Zeiss Ultra 55', [viewed 2015 17.3.]; Available from: http://portal.tugraz.at/portal/page/portal/felmi/instrumentation/Ultra55.
37. E. Verdonck, K. Schaap, and L. C. Thomas, *International Journal of Pharmaceutics*, 1999, 192(1), 3-20.
38. F. Köln. 'Thermische Analyse', 24.03.2009 [viewed 2014 12.10]; Available from: http://www.gm.fh-koeln.de/~werkst/Hauptseiten/DSC-DIL_oK.pdf.
39. M. Klein, F. Kuhlmann, P. Wittke, H. Dieringa, and F. Walther, *Materials and Corrosion*, 2014.
40. M. P. Liu, Q. D. Wang, Z. L. Liu, G. Y. Yuan, G. H. Wu, Y. P. Zhu, and W. J. Ding, *Journal of Materials Science Letters*, 2002, 21(16), 1281-1283.
41. L. Han, H. Hu, D. O. Northwood, and N. Li, *Materials Science and Engineering: A*, 2008, 473(1–2), 16-27.
42. K. P. Rao, H. Y. Ip, K. Suresh, Y. V. R. K. Prasad, C. M. L. Wu, N. Hort, and K. U. Krainer, *Philosophical Magazine*, 2013, 93, 4364-4377.
43. Elettra. 'Elettra and Fermi lightsources', [viewed 2015 16.07.]; Available from: https://www.elettra.trieste.it/.